

## SDSS+JWST Census of Stellar and Nebular Dust Attenuation at $z \sim 0-7$ : Mass Dependence and Redshift Evolution

JIE SONG <sup>1,2,3</sup> MASAMI OUCHI <sup>3,4,5,6</sup> TOMOKAZU KIYOTA <sup>5,6</sup> CHENGHAO ZHU <sup>3,7</sup> XU KONG <sup>1,2,8</sup> AND  
YURINA NAKAZATO <sup>9</sup>

<sup>1</sup>*Department of Astronomy, University of Science and Technology of China, Hefei 230026, China*

<sup>2</sup>*School of Astronomy and Space Science, University of Science and Technology of China, Hefei 230026, China*

<sup>3</sup>*Institute for Cosmic Ray Research, The University of Tokyo, 5-1-5 Kashiwanoha, Kashiwa, Chiba 277-8582, Japan*

<sup>4</sup>*Kavli Institute for the Physics and Mathematics of the Universe (WPI), University of Tokyo, Kashiwa, Chiba 277-8583, Japan*

<sup>5</sup>*Department of Astronomical Science, The Graduate University for Advanced Studies, SOKENDAI, 2-21-1 Osawa, Mitaka, Tokyo, 181-8588, Japan*

<sup>6</sup>*National Astronomical Observatory of Japan, 2-21-1 Osawa, Mitaka, Tokyo, 181-8588, Japan*

<sup>7</sup>*Department of Physics, Graduate School of Science, The University of Tokyo, 7-3-1 Hongo, Bunkyo, Tokyo 113-0033, Japan*

<sup>8</sup>*Institute of Deep Space Sciences, Deep Space Exploration Laboratory, Hefei 230026, China*

<sup>9</sup>*Center for Computational Astrophysics, Flatiron Institute, 162 5th Avenue, New York, NY 10010*

### ABSTRACT

We present the demography of dust attenuation, including its mass dependence and redshift evolution, using spectroscopic samples of 34,182 SDSS galaxies at  $z \sim 0.1$  and 863 JWST/JADES galaxies at  $z \sim 1.5-7$ . We find that, on average, H $\alpha$ /H $\beta$  ratios are comparable to the Case B recombination value at  $M_* \lesssim 10^9 M_\odot$ , and increase beyond  $M_* \sim 10^9 M_\odot$  both at  $z \sim 0.1$  and  $1.5-7$ . We derive the nebular attenuation  $A_{V,\text{nebular}}$  from Balmer decrements and the stellar attenuation  $A_{V,\text{stellar}}$  from rest-frame UV-optical spectra with supplementary *GALEX* data, via comparisons with stellar-population models and multiple attenuation curves in a consistent manner across cosmic time. We find no significant redshift evolution of  $A_{V,\text{nebular}}$  and  $A_{V,\text{stellar}}$  at fixed  $M_*$  over  $z \sim 0-7$ , forming a universal extinction relation, and both rise from 0.2-0.4 at  $M_* \lesssim 10^9 M_\odot$  to  $\sim 1$  at  $M_* \sim 10^{11} M_\odot$ . Interestingly, at  $M_* \gtrsim 10^9 M_\odot$ ,  $A_{V,\text{nebular}}$  rises more steeply than  $A_{V,\text{stellar}}$ . This correlation holds within an uncertainty of  $\sim \pm 0.2$  for various combinations of attenuation curves (Calzetti, SMC, and Milky Way). These results indicate that  $M_* \sim 10^9 M_\odot$  is a transition mass in dust attenuation, whose low-mass behavior reflects dust widely distributed by feedbacks. These mass-dependent extinction results address the long-standing issue of appropriate choice of the stellar-to-nebular color excess ratio,  $f \equiv E(B-V)_{\text{stellar}}/E(B-V)_{\text{nebular}} = 1.0$  or 0.44, and suggest that galaxy  $M_*$  determines  $f$  from  $\sim 1.0$  to  $\sim 0.44$  across low- to high-mass galaxies.

*Keywords:* Galaxy evolution (594) — High-redshift galaxies (734) — Interstellar dust extinction (837)

### 1. INTRODUCTION

Dust attenuation is one of the most fundamental physical processes in extragalactic astronomy, fundamentally affecting the derivation of galaxy physical properties, such as stellar masses ( $M_*$ ) and star formation rates (SFRs), across all cosmic epochs (e.g., Kennicutt 1998; Calzetti et al. 2000; Charlot & Fall 2000; Kennicutt & Evans 2012; Aoyama et al. 2017; Galliano et al. 2018). Interstellar dust grains absorb and scatter ultraviolet (UV) and optical photons emitted by stars and ionized gas and subsequently re-radiate the absorbed energy at

far-infrared wavelengths (e.g., Dole et al. 2006; Draine 2011; Viero et al. 2013; Galliano et al. 2018). This process biases virtually every observable quantity derived from short-wavelength light. Accurately characterizing dust attenuation is therefore essential for understanding the overall formation and evolution of galaxies.

Numerous previous studies have demonstrated that galactic dust attenuation is affected by the total dust content, grain size distribution, and chemical composition (e.g., Mathis et al. 1977; Weingartner & Draine 2001; Draine 2011; Asano et al. 2013b; Aoyama et al. 2020; Salim & Narayanan 2020; Matsumoto et al. 2026).

Furthermore, the geometry between dust and stars is also believed to be an important factor governing dust attenuation, as dust is not necessarily uniformly distributed within galaxies (e.g., Calzetti 1997; Charlot & Fall 2000; Popping et al. 2017; Narayanan et al. 2018; Koyama et al. 2019; Vijayan et al. 2024; Nakazato et al. 2026). This non-uniform distribution has been examined in a series of observational studies (e.g., Calzetti et al. 1994; Calzetti 1997; Calzetti et al. 2000; Kashino et al. 2013; Price et al. 2014; Reddy et al. 2015; Karthikeyan et al. 2026), which have revealed that the attenuation experienced by the stellar continuum,  $A_{V,\text{stellar}}$ , differs systematically from that experienced by the ionized gas,  $A_{V,\text{nebular}}$ , motivating the non-standard practice of treating  $A_{V,\text{stellar}}$  and  $A_{V,\text{nebular}}$  as distinct quantities.

The stellar continuum attenuation can be derived from spectral energy distribution (SED) fitting, the rest-frame UV slope, or the infrared excess (e.g., Kong et al. 2004; McLure et al. 2018; Galliano et al. 2018; Woodrum et al. 2025). In previous works,  $M_*$  of a galaxy has been identified as a robust proxy of the dust attenuation affecting its UV emission over a broad redshift range (e.g., Pannella et al. 2009; Kashino et al. 2013; Oteo et al. 2014; Pannella et al. 2015), reflecting the expectation that the dust content of a galaxy grows together with its assembled  $M_*$ . Although some studies have found that high-redshift galaxies host less dust than their local counterparts of similar mass (e.g., Shivaeei et al. 2022; Jolly et al. 2025; Bakx 2026), many other works have shown that the  $A_{V,\text{stellar}}-M_*$  relation does not evolve significantly with redshift at fixed  $M_*$ , at least out to  $z \sim 3$  (e.g., Pannella et al. 2015; Whitaker et al. 2017; McLure et al. 2018). For instance, using a sample at  $0 < z < 2.5$ , Whitaker et al. (2017) found that the obscured fraction of star formation is approximately 50% at  $\log(M_*/M_\odot) = 9.4$  and exceeds 90% above  $\log(M_*/M_\odot) = 10.5$  at all redshifts, providing evidence that the  $A_{V,\text{stellar}}-M_*$  relation is robust across cosmic noon. However, less consensus has been reached at higher redshifts (e.g., Fudamoto et al. 2020; Algera et al. 2023; Wijesekera et al. 2026).

For  $A_{V,\text{nebular}}$ , the most common approach is to infer it from the Balmer decrement (hereafter BD)  $H\alpha/H\beta$  under the assumption of Case B recombination. As with  $A_{V,\text{stellar}}$ , a number of studies have established that  $M_*$  is the dominant galaxy property setting  $A_{V,\text{nebular}}$  (e.g., Brinchmann et al. 2004; Garn & Best 2010; Shapley et al. 2022, 2023; Sandles et al. 2024; Woodrum et al. 2025). For example, Garn & Best (2010) found that, after controlling for  $M_*$ , no residual correlation with SFR or metallicity remains using a sample from Sloan Digi-

tal Sky Survey (SDSS, Abazajian et al. 2009). Although numerous studies have demonstrated that the dust content of galaxies correlates with various physical properties (e.g., Tacconi et al. 2018; Li et al. 2019; Sanders et al. 2021), the  $A_{V,\text{nebular}}-M_*$  relation has been found to remain nearly invariant from  $z \sim 7$  to  $z \sim 0$  at fixed  $M_*$ .

The difference between  $A_{V,\text{nebular}}$  and  $A_{V,\text{stellar}}$ , which encodes the spatial distribution of stars relative to dust within galaxies, is considerably more complex. The canonical empirical relationship between  $A_{V,\text{stellar}}$  and  $A_{V,\text{nebular}}$  originates from the work of Calzetti (1997), who found  $f = 0.44$ , where  $f$  is defined as:

$$f \equiv E(B - V)_{\text{stellar}}/E(B - V)_{\text{nebular}} \quad (1)$$

This is still widely adopted in some recent studies (e.g., Mehta et al. 2023). A physical explanation for this differential attenuation is provided by the two-component dust model (Charlot & Fall 2000; Wild et al. 2011; Chevillard et al. 2013), which remains the standard theoretical framework for interpreting  $f$  to this day. In the model of Charlot & Fall (2000), the interstellar medium (ISM) is composed of a diffuse ISM component and dense molecular birth clouds. Stars younger than  $\sim 10^7$  yr remain embedded within optically thick birth clouds and experience attenuation from both components, while older stars have migrated out of their natal clouds and are attenuated only by the diffuse ISM. Because nebular emission lines arise exclusively from H II regions surrounding massive O and B stars still inside birth clouds, the nebular emission is always more attenuated than the integrated stellar continuum, naturally producing  $f < 1$  without requiring any special dust geometry.

However, analyses of large statistical samples in the local universe have demonstrated that  $f$  is not a universal constant, indicating that the differential attenuation between the nebular and stellar components varies systematically with galaxy physical properties (e.g., Wild et al. 2011; Zahid et al. 2017; Koyama et al. 2019; Lin & Kong 2020; Li et al. 2021). In particular, early studies using two-component models demonstrated that the relative contributions of young and old stellar populations, which are tightly regulated by the specific SFR, strongly dictate the integrated differential dust attenuation (Kong et al. 2004). For example, by combining Wide-field Infrared Survey Explorer (WISE, Wright et al. 2010), SDSS, and Galaxy Evolution Explorer (GALEX, Martin et al. 2005) photometry for more than 50,000 local galaxies at  $0.02 < z < 0.10$ , Koyama et al. (2019) revealed that  $f$  decreases with  $M_*$  and increases with sSFR.

At higher redshift, the conclusions regarding differential dust attenuation become increasingly complex, with a diverse range of  $f$  values reported in the literature (e.g., Kashino et al. 2013; Wuyts et al. 2013; Price et al. 2014; Pannella et al. 2015; Woodrum et al. 2025; Lorenz et al. 2025; Tsujita et al. 2026; Karthikeyan et al. 2026). Utilizing a sample of 473 galaxies from the 3D-HST survey at  $0.7 < z < 1.5$ , Wuyts et al. (2013) reported a result consistent with the local Calzetti (1997) relation, while Puglisi et al. (2016) reported a value of  $f \approx 0.93$  at  $z \sim 1$  also based on a 3D-HST sample. However, in another study using a sample from the COSMOS field, Kashino et al. (2013) found  $f \approx 0.7\text{--}0.83$  at  $z \sim 1.6$ . Moreover, several investigations have revealed that this differential attenuation continues to exhibit dependencies on galaxy  $M_*$  within this redshift regime (e.g., Price et al. 2014; Reddy et al. 2015; Karthikeyan et al. 2026).

This variable  $f$  implies that, although both  $A_{V,\text{nebular}}$  and  $A_{V,\text{stellar}}$  correlate with  $M_*$ , their dependences on  $M_*$  are not identical. A more careful and systematic characterization of how  $A_{V,\text{nebular}}$ ,  $A_{V,\text{stellar}}$ , and their difference depend on  $M_*$ , and how each evolves with redshift, is therefore necessary. Although significant progress has been made in previous studies, a number of important questions remain open. First, measuring  $A_{V,\text{nebular}}$  requires the BD. At high redshift, the H $\alpha$  emission line is redshifted into the observed-frame near-infrared, a wavelength regime that was largely inaccessible for statistical galaxy samples prior to the advent of the *James Webb Space Telescope* (JWST). Detailed studies of these questions at  $z > 3$  are therefore still very limited (e.g., Woodrum et al. 2025; Karthikeyan et al. 2026; Tsujita et al. 2026; Reddy et al. 2026). Second, prior work has focused on different redshift ranges and adopted a wide variety of methods to derive  $A_{V,\text{stellar}}$ , often in conjunction with different assumptions about the stellar population templates (e.g., Kashino et al. 2013; Price et al. 2014; Puglisi et al. 2016). This methodological heterogeneity makes direct, quantitative comparisons across studies difficult. A systematic study characterizing  $A_{V,\text{nebular}}$ ,  $A_{V,\text{stellar}}$ , and their difference across a wide range of redshifts using a self-consistent methodology has hitherto been lacking.

In this paper, we present a systematic census of nebular and stellar dust attenuation from  $z \sim 0$  to  $z \sim 7$ , utilizing a combined sample of 34,182 SDSS+GALEX star-forming galaxies at  $z \sim 0.1$  and 863 JWST galaxies at  $z \sim 1.5\text{--}7$ , analyzed with a fully self-consistent methodology. We derive  $A_{V,\text{stellar}}$  from SED fitting with the `Bagpipes` code (Carnall et al. 2018, 2019), adopting identical priors for both samples to ensure uniformity. Simultaneously,  $A_{V,\text{nebular}}$  is estimated from

the observed BD, facilitating a self-consistent comparison across cosmic time. We find that both  $A_{V,\text{nebular}}$  and  $A_{V,\text{stellar}}$  correlate positively with  $M_*$  and show no significant redshift evolution. Moreover,  $A_{V,\text{nebular}}$  increases more steeply with  $M_*$  than  $A_{V,\text{stellar}}$  for galaxies with  $\log(M_*/M_\odot) \gtrsim 9$ . Consequently,  $f$  approaches 1.0 at  $\log(M_*/M_\odot) \lesssim 9$  and decreases monotonically toward the canonical value of 0.44 above this threshold, with no statistically significant redshift evolution from  $z \sim 7$  to  $z \sim 0$  at fixed  $M_*$ .

The structure of this paper is as follows. In Section 2, we detail the dataset construction and sample selection criteria. Section 3 outlines our procedures for deriving the nebular and stellar dust attenuation, respectively. We present our main results in Section 4. Section 5 explores the sensitivity of our findings to the assumed dust attenuation curve and provides a possible physical interpretation of our results. Finally, a summary of our conclusions is given in Section 6. Throughout this work, we assume a Kroupa (2001) initial mass function and adopt a flat  $\Lambda$ CDM cosmology characterized by  $H_0 = 70 \text{ km s}^{-1} \text{ Mpc}^{-1}$ ,  $\Omega_m = 0.3$ , and  $\Omega_\Lambda = 0.7$ .

## 2. DATASET AND SAMPLE SELECTION

### 2.1. SDSS-GALEX

We constructed our low-redshift sample by leveraging the synergy between two large surveys: SDSS DR8 (York et al. 2000; Aihara et al. 2011), which provides optical imaging and spectroscopy, and GALEX GR6 (Martin et al. 2007), which offers the ultraviolet coverage needed to constrain young stellar populations.

Our parent optical sample is drawn from the MPA-JHU DR8 Value-Added Catalog<sup>10</sup> (Kauffmann et al. 2003a; Brinchmann et al. 2004; Tremonti et al. 2004). We restricted the redshift range to  $0.05 < z < 0.10$  (hereafter, we adopt  $z \sim 0.1$  to represent this redshift range) to minimize fiber aperture effects. To guarantee the reliability of the derived physical properties, we excluded objects with uncertain redshifts or unreliable emission-line measurements by requiring `z_warning=0` and `reliable=1`. To ensure robust estimates of nebular dust extinction via BD, we further imposed a signal-to-noise ratio (S/N) cut of  $S/N > 5$  for both the H $\alpha$  and H $\beta$  emission lines.

To isolate star-forming galaxies and remove contamination from active galactic nuclei (AGN), we used the BPT diagram (Baldwin et al. 1981) and selected star-forming galaxies following the separation line defined by Kauffmann et al. (2003b). These criteria yielded an ini-

<sup>10</sup> [https://www.sdss4.org/dr17/spectro/galaxy\\_mpa\\_jhu/](https://www.sdss4.org/dr17/spectro/galaxy_mpa_jhu/)

tial optical sample of 76,758 galaxies. For these objects, we adopted the emission-line flux measurements from the MPA-JHU catalog, while the corresponding optical spectra and broadband photometry were retrieved from the SDSS Science Archive Server<sup>11</sup> and the SDSS CasJobs site<sup>12</sup>, respectively.

The wavelength coverage of the SDSS spectra spans 3800–9200 Å. Some previous studies have suggested that optical data alone may not fully break the degeneracy between age, dust, and metallicity (e.g., Pforr et al. 2012; Salim et al. 2016). Other works, however, have shown that stellar population properties derived from optical-only spectral fitting are broadly consistent with those obtained from joint optical–UV analyses (e.g., López Fernández et al. 2016). To be conservative, we incorporated UV data to obtain more robust results in this work. To this end, we retrieved UV photometry in the FUV and NUV bands via the GALEX CasJobs server<sup>13</sup>. Following the matching methodology recommended by Budavári et al. (2009), we cross-matched each SDSS source with the nearest GALEX detection within a search radius of 3". This process yielded a final low-redshift sample of 34,182 star-forming galaxies with UV detections.

## 2.2. JADES

To investigate dust attenuation properties in the high-redshift universe, we drew our sample from the JWST Advanced Deep Extragalactic Survey (JADES, Eisenstein et al. 2023). JADES is a comprehensive survey targeting the GOODS-S and GOODS-N fields, providing deep near-infrared imaging and spectroscopy with high sensitivity. For a detailed description of the survey design, data reduction, and data products, we refer the reader to the JADES data release papers (Bunker et al. 2024; Hainline et al. 2024; Rieke et al. 2023; Eisenstein et al. 2025; D’Eugenio et al. 2025; Curtis-Lake et al. 2025; Scholtz et al. 2025a; Robertson et al. 2026).

The spectroscopic observations used in this work were obtained with the NIRSpec Micro-Shutter Assembly in Multi-Object Spectroscopy mode (Jakobsen et al. 2022; Ferruit et al. 2022; Böker et al. 2023). The survey strategy employs both the low-resolution prism (PRISM/CLEAR;  $R \sim 100$ ) and the medium-resolution gratings (G140M/F070LP, G235M/F170LP, and G395M/F290LP;  $R \sim 1000$ ). We retrieved the fully

**Table 1.** The SED fitting parameters and their priors used in this work

Parameter	Limits	Prior
$z$	$(z_{\text{spec}} - 0.01, z_{\text{spec}} + 0.01)$	Uniform
$\log(M_{*,\text{form}}/M_{\odot})$	(4, 13)	Uniform
$Z/Z_{\odot}$	(1e−4, 10)	Logarithmic
$\log U$	(−4, 0)	Uniform
$A_V$	(0, 4)	Uniform

reduced spectroscopic data from the Mikulski Archive for Space Telescopes (MAST)<sup>14</sup>.

Our high-redshift sample is constructed from the spectroscopic catalogs of JADES DR4 (Scholtz et al. 2025a). To deblend the H $\alpha$  emission line from the [N II] doublet, we used emission-line fluxes derived from the medium-resolution grating observations. We restricted our analysis to galaxies in the redshift range  $1.5 < z < 7.0$ . Consistent with our low-redshift selection criteria, we required S/N > 5 for both the H $\alpha$  and H $\beta$  emission lines. To account for slit-loss effects, we also retrieved the corresponding photometric catalogs from MAST and required that all selected galaxies have valid NIRCcam observations.

To remove potential contamination from AGN, we performed a careful exclusion procedure based on the following criteria. First, for galaxies with detections of both [O III] and [N II], we rejected sources falling in the AGN region of the BPT diagram (Baldwin et al. 1981) following the criterion of Kauffmann et al. (2003b). Second, we cross-checked our sample against the literature and excluded known broad-line and narrow-line AGNs reported in these fields (Juodžbalis et al. 2025; Scholtz et al. 2025b). Finally, we cross-matched our sources with deep X-ray catalogs in the GOODS-S and GOODS-N fields (Xue et al. 2016; Lyu et al. 2022) and rejected any objects with X-ray counterparts. After applying these criteria, our final high-redshift sample consists of 863 star-forming galaxies.

## 3. ANALYSIS

### 3.1. $A_{V,\text{stellar}}$ Measurements

In this work, we used **Bagpipes** to measure the  $M_*$  and  $A_{V,\text{stellar}}$  of the SDSS and JADES galaxies via SED fitting. Before proceeding with the SED fitting analysis, and following the method adopted by the MPA-JHU group, the observed data were corrected for Galactic extinction using the Schlafly & Finkbeiner (2011) dust maps and the O’Donnell (1994) attenuation curve.

<sup>11</sup> <http://dr8.sdss.org/home>

<sup>12</sup> <https://skyserver.sdss.org/CasJobs/default.aspx>

<sup>13</sup> <https://galex.stsci.edu/casjobs/default.aspx>

<sup>14</sup> <https://archive.stsci.edu/hlsp/jades>

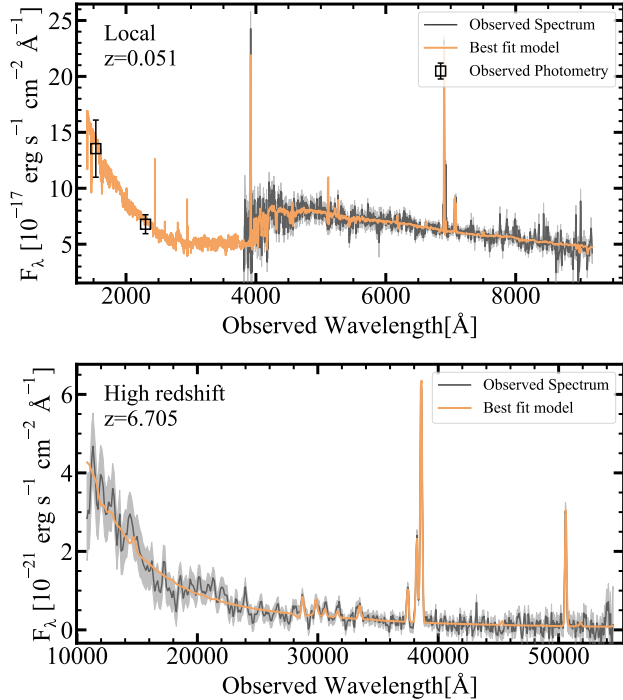


**Figure 1.** Top panel: SED fitting example from the SDSS sample; bottom panel: SED fitting example from the JADES sample. The black solid line and gray shaded region show the observed spectrum and its uncertainty, respectively, and the yellow solid line shows the best-fit model. The black squares with error bars denote the observed GALEX UV photometry and associated uncertainties.

For the SDSS sample, following the methodology of Werle et al. (2019), we simultaneously fit the GALEX UV photometry and the SDSS optical spectra. During the fitting process, we assumed a non-parametric star formation history (SFH) with a Student- $t$  distribution acting as a continuity prior (e.g., Leja et al. 2019; Tacchella et al. 2022). The SFH is divided into six time bins: the two most recent bins are fixed at 0–3 Myr and 3–10 Myr, while the remaining four are logarithmically spaced in time back to the beginning of the Universe. To account for dust, we tested various attenuation and extinction laws, including the Calzetti et al. (2000) curve (hereafter CAL), the Small Magellanic Cloud attenuation curve (hereafter SMC) of Gordon et al. (2003), and the Milky Way extinction curve (hereafter MW) of Cardelli et al. (1989). All other SED fitting parameters and adopted priors are summarized in Table 1. To recover the total physical properties of each galaxy, we applied an aperture correction to the fitting results based on the difference between the total and fiber-based  $r$ -band magnitudes (e.g., Kewley et al. 2005; Koyama et al. 2019).

For the JADES sample, we fit the full JWST/NIRSpec PRISM spectra, masking rest-frame wavelengths below 1400 Å to exclude the Ly $\alpha$  damping region (Heintz et al. 2025) and short-wavelength instrumental effects. Following the method described in Markov et al. (2025), we also applied a slit-loss correction to the JADES spectra by scaling them according to the difference between the photometric and spectroscopic flux densities for each source. The priors adopted in the SED fitting are the same as those used for the SDSS sample. Figure 1 shows two representative examples of our SED fitting results for the SDSS (top panel) and JADES (bottom panel) samples. As shown in Figure 1, the spectral features are well reproduced by our fits.

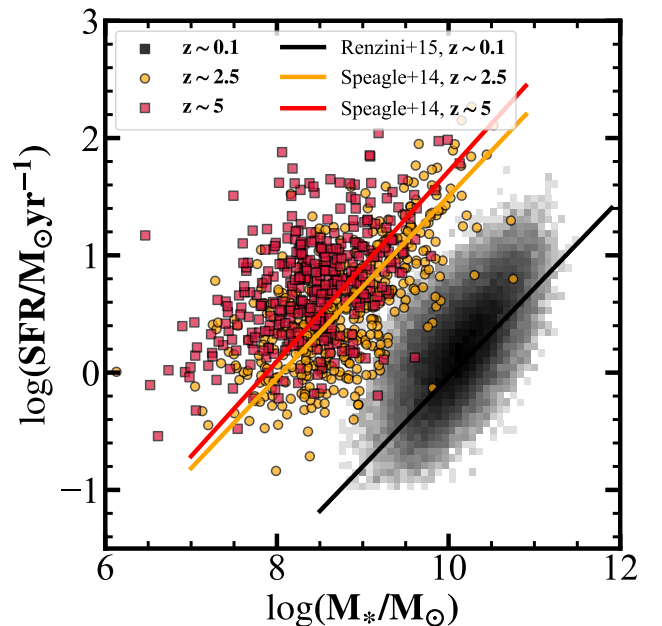


**Figure 2.** Distribution of our sample in the SFR– $M_*$  plane. Black two-dimensional histogram show the result for our local sample, while orange and red symbols show the result for galaxies at  $1.5 < z < 3.5$  and  $3.5 < z < 7$ , respectively. For comparison, SFMS at  $z \sim 0.1$  from Renzini & Peng (2015) and at  $z \sim 2.5$  and  $z \sim 5$  from Speagle et al. (2014), are shown as black, orange, and red solid lines, respectively.

Table 2. Part of The Final Catalogue

ID	RA (deg)	DEC (deg)	z	CAL Curve			MW Curve			SMC Curve					
				$\log M_*$	$A_{V,stellar}$	$A_{V,nebular}$	SFR	$\log M_*$	$A_{V,stellar}$	$A_{V,nebular}$	SFR	$\log M_*$	$A_{V,stellar}$	$A_{V,nebular}$	SFR
(1)	(2)	(3)	(4)	(5)	(6)	(7)	(8)	(9)	(10)	(11)	(12)	(13)	(14)	(15)	(16)
SDSS Sample															
299493800143775744	146.63167	-0.98828	0.053	9.50 ± 0.02	0.80 ± 0.04	0.36 ± 0.23	0.21 ± 0.01	9.46 ± 0.02	0.76 ± 0.04	0.33 ± 0.21	0.21 ± 0.01	9.51 ± 0.02	0.58 ± 0.03	0.27 ± 0.17	0.20 ± 0.01
299529809149585408	146.35204	-0.33269	0.052	10.39 ± 0.01	1.14 ± 0.03	1.81 ± 0.08	5.19 ± 0.11	10.30 ± 0.01	0.89 ± 0.03	1.65 ± 0.07	4.56 ± 0.09	10.29 ± 0.01	1.07 ± 0.03	1.34 ± 0.06	3.50 ± 0.05
299553107684468736	146.39902	-0.35038	0.054	9.74 ± 0.01	1.43 ± 0.02	1.61 ± 0.13	1.43 ± 0.05	9.70 ± 0.01	1.25 ± 0.02	1.46 ± 0.12	1.27 ± 0.04	9.64 ± 0.01	1.18 ± 0.02	1.19 ± 0.10	1.01 ± 0.02
299572690103068672	145.32060	-0.25286	0.052	10.23 ± 0.00	0.85 ± 0.02	0.95 ± 0.11	1.07 ± 0.02	10.16 ± 0.01	0.53 ± 0.01	0.86 ± 0.10	1.00 ± 0.02	10.13 ± 0.00	0.52 ± 0.01	0.70 ± 0.08	0.87 ± 0.01
299604301062367232	145.89355	1.02842	0.053	10.21 ± 0.01	0.71 ± 0.02	1.26 ± 0.18	1.40 ± 0.03	10.15 ± 0.01	0.68 ± 0.02	1.14 ± 0.16	1.28 ± 0.03	10.18 ± 0.01	0.79 ± 0.02	0.93 ± 0.13	1.07 ± 0.02
299491051834468352	146.63167	-0.98828	0.053	9.44 ± 0.01	0.61 ± 0.04	0.52 ± 0.22	0.26 ± 0.01	9.43 ± 0.01	0.55 ± 0.04	0.47 ± 0.20	0.25 ± 0.01	9.44 ± 0.01	0.48 ± 0.03	0.38 ± 0.16	0.23 ± 0.01
JADES Sample															
goods-s-mediumhst_2430	53.12819	-27.78769	5.481	7.40 ± 0.15	0.32 ± 0.11	0.21 ± 0.52	4.00 ± 1.20	7.33 ± 0.10	0.24 ± 0.08	0.19 ± 0.48	3.94 ± 1.08	7.31 ± 0.10	0.15 ± 0.05	0.16 ± 0.39	3.82 ± 0.83
goods-s-deephst_2923	53.15407	-27.82094	3.014	7.80 ± 0.07	0.11 ± 0.06	0.00 ± 0.50	0.82 ± 0.16	7.87 ± 0.05	0.03 ± 0.03	0.00 ± 0.46	0.82 ± 0.14	7.85 ± 0.06	0.04 ± 0.02	0.00 ± 0.37	0.82 ± 0.11
goods-s-mediumjwst_3049	53.07061	-27.90819	3.469	8.38 ± 0.09	0.48 ± 0.06	0.29 ± 0.33	3.43 ± 0.52	8.35 ± 0.09	0.39 ± 0.05	0.26 ± 0.30	3.36 ± 0.46	8.35 ± 0.09	0.24 ± 0.03	0.22 ± 0.24	3.22 ± 0.35
goods-s-deephst_3184	53.15010	-27.81971	3.466	8.57 ± 0.05	0.50 ± 0.02	0.10 ± 0.27	2.97 ± 0.26	8.81 ± 0.01	0.11 ± 0.01	0.09 ± 0.25	2.95 ± 0.23	8.89 ± 0.03	0.13 ± 0.01	0.07 ± 0.20	2.91 ± 0.18
goods-s-mediumjwst_3191	53.06071	-27.90770	2.567	8.95 ± 0.03	0.34 ± 0.12	0.00 ± 0.63	0.53 ± 0.14	8.93 ± 0.03	0.24 ± 0.10	0.00 ± 0.57	0.53 ± 0.13	8.91 ± 0.03	0.31 ± 0.09	0.00 ± 0.47	0.53 ± 0.10
goods-s-deephst_3334	53.15138	-27.81917	6.705	7.45 ± 0.15	0.04 ± 0.04	0.00 ± 0.59	1.07 ± 0.39	7.44 ± 0.17	0.08 ± 0.05	0.00 ± 0.53	1.07 ± 0.35	7.45 ± 0.14	0.02 ± 0.02	0.00 ± 0.43	1.07 ± 0.29

NOTE—(1) Source ID, corresponding to the SPEC0BJD from the MPA-JHU DR8 catalog for the SDSS sample, and the `unique_id` from the JADES DR4 catalog for the JADES sample; (2) R.A. in decimal degrees; (3) Decl. in decimal degrees; (4) Spectroscopic redshift; (5)–(8) Stellar mass ( $\log M_*/M_\odot$ ),  $A_{V,nebular}$ , and SFR derived assuming a CAL attenuation curve; (9)–(12) Same as (5)–(8), but assuming a MW extinction curve; (13)–(16) Same as (5)–(8), but assuming a SMC extinction curve.

### 3.2. $A_{V,\text{nebular}}$ Measurements

We derived  $A_{V,\text{nebular}}$  for each galaxy from BD. The relevant relations are

$$E(B - V)_{\text{nebular}} = \frac{2.5}{\kappa(\text{H}\beta) - \kappa(\text{H}\alpha)} \log\left(\frac{R_{\text{obs}}}{R_{\text{int}}}\right) \quad (2)$$

$$A_{V,\text{nebular}} = R_V \times E(B - V)_{\text{nebular}} \quad (3)$$

where  $\kappa(\text{H}\alpha)$  and  $\kappa(\text{H}\beta)$  are the values of the attenuation curve at the wavelengths of  $\text{H}\alpha$  and  $\text{H}\beta$ , respectively,  $R_{\text{obs}} \equiv F_{\text{H}\alpha}/F_{\text{H}\beta}$  is the observed BD, and  $R_{\text{int}}$  is the intrinsic BD assumed for the ionized gas.

For the SDSS sample, we adopted the widely used assumption of Case B recombination with an electron density of  $n_e = 10^2 \text{ cm}^{-3}$  and a temperature of  $T_e = 10^4 \text{ K}$ , yielding  $R_{\text{int}} = 2.86$  (e.g., Osterbrock 1989; Brinchmann et al. 2004). However, recent studies have shown that this assumption, calibrated in the local Universe, may not be appropriate at high redshift (e.g., Shapley et al. 2023; Sandles et al. 2024; Cameron et al. 2024). For the JADES sample, we therefore adopted the conditions suggested by Reddy et al. (2023), characterized by  $T_e = 15,000 \text{ K}$  and  $n_e = 100 \text{ cm}^{-3}$ , which correspond to  $R_{\text{int}} = 2.79$ .

For  $A_{V,\text{nebular}}$ , we also considered multiple dust attenuation curves, including the CAL, SMC, and MW curves. We note that a subset of galaxies in our sample exhibit observed BD below the theoretical intrinsic value. While this could reflect departures from Case B recombination (e.g., Yanagisawa et al. 2024; Topping et al. 2024; McClymont et al. 2025), it is more likely attributable to measurement uncertainty in galaxies whose intrinsic BD lie close to the theoretical floor, causing the observed ratio to scatter below the theoretical value (e.g., Lin & Yan 2024). For these galaxies, we set  $E(B - V)_{\text{nebular}} = 0$  to represent their intrinsically low dust attenuation.

We then applied an aperture correction to the dust-corrected  $\text{H}\alpha$  flux based on the difference between the total photometric flux of each galaxy and the synthetic flux derived from the spectra, following the method described in Koyama et al. (2019) and Clarke et al. (2024). From the aperture-corrected  $\text{H}\alpha$  flux, we derived SFR using the calibration of Kennicutt (1998). The results derived here, together with those obtained from the SED fitting described above, will be made available online. Representative examples of our derived parameters are presented in Table 2.

Although we have computed  $A_{V,\text{stellar}}$  and  $A_{V,\text{nebular}}$  under multiple assumed dust attenuation curves, numerous studies have demonstrated that the CAL law provides a robust description of the integrated attenuation for the stellar continuum in star-forming galaxies

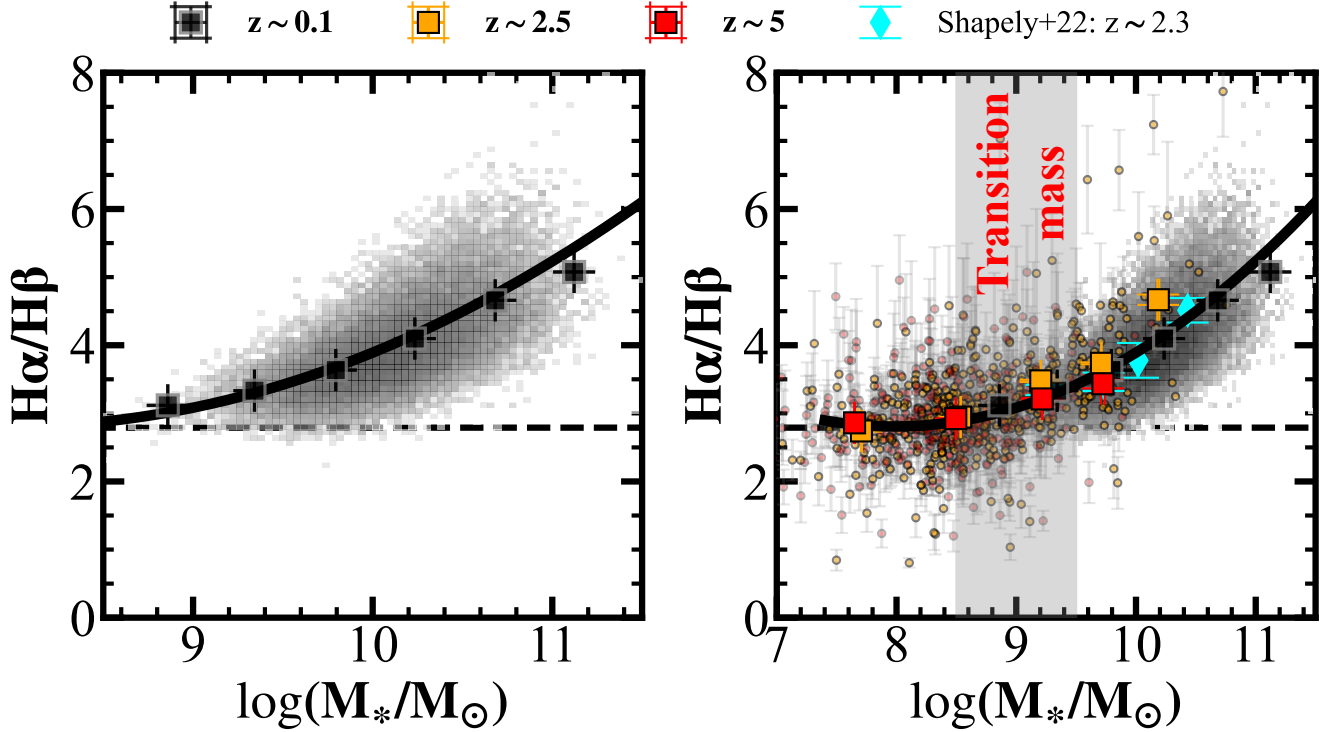
at both low (e.g., Calzetti et al. 2000; Battisti et al. 2016, 2017) and high redshifts (e.g., Rodighiero et al. 2026). For the nebular component, the MW extinction curve with  $R_V = 3.1$  has been similarly well-supported across cosmic time (e.g., Reddy et al. 2015; Rezaee et al. 2021). Furthermore, the combination of a CAL-like stellar attenuation curve and a MW-like nebular extinction curve remains the most widely adopted convention in the existing literature (e.g., Calzetti 1997; Koyama et al. 2019). Consequently, we adopt  $A_{V,\text{stellar}}$  from the CAL law and  $A_{V,\text{nebular}}$  from the MW curve as our fiducial measurements, and present the results derived from this combination in the following sections. A detailed discussion of the impact of alternative attenuation curves is provided in Section 5.1.

Figure 2 shows the distribution of our sample in the SFR– $M_*$  plane. Because our JADES sample spans a broad redshift range, we divide it into two redshift bins,  $1.5 < z < 3.5$  (491 galaxies) and  $3.5 < z < 7$  (372 galaxies), for the analyses that follow (hereafter, we adopt  $z \sim 2.5$  and  $z \sim 5$  to represent these two redshift ranges). For reference, we also overlay the star-forming main sequence (SFMS) at  $z \sim 0.1$  from Renzini & Peng (2015), together with the relations at  $z \sim 2.5$  and  $z \sim 5$  from Speagle et al. (2014) in Figure 2. As is evident from this comparison, our sample predominantly follows the SFMS across all redshift bins.

## 4. GALAXY DUST PROPERTIES

### 4.1. $A_{V,\text{nebular}}$ and $A_{V,\text{stellar}}$

We first examine how galactic dust attenuation varies with  $M_*$ . The most direct approach to this question is the relation between the BD and  $M_*$ , because the BD is a directly observed quantity that does not rely on stellar-population modeling. Previous studies have established that the BD increases monotonically with  $M_*$ , and that this relation exhibits little to no evolution with redshift (e.g., Garn & Best 2010; Domínguez et al. 2013; Shapley et al. 2022, 2023; Sandles et al. 2024; Woodrum et al. 2025). In this study, we revisit this relation by combining the SDSS and JADES samples, and the results are presented in Figure 3. The left panel shows the SDSS results, while the right panel presents the results from JADES together with those from SDSS. The black two-dimensional histogram illustrates the result at  $z \sim 0.1$ , while orange and red circles represent the results at  $z \sim 2.5$  and  $z \sim 5$ , respectively. Squares denote the mean values within each  $M_*$  bin, with error bars representing the corresponding standard error. The black dashed line indicates the theoretical BD of 2.79 adopted for the JADES sample. For comparison, the results at



**Figure 3.** The distribution of BD as a function of  $M_*$ . The left panel shows the SDSS results, and the right panel shows the JADES results together with the SDSS results. The black, orange, and red symbols represent results at  $0.05 < z < 0.1$ ,  $1.5 < z < 3.5$ , and  $3.5 < z < 7$ , respectively. Squares denote the median values in bins of  $M_*$ , while the error bars indicate the standard error within each bin. The black dashed line represents the theoretical value 2.79 under Case B recombination. The best-fitting result is represented by the solid black line. Shaded gray region represents the transition mass at  $\log(M_*/M_\odot) = 9$ . For comparison, we also show the results from [Shapley et al. \(2022\)](#) at  $z \sim 2.3$  as cyan diamonds. It can be seen from this figure, at fixed  $M_*$ , BD exhibits little to no evolution with redshift.

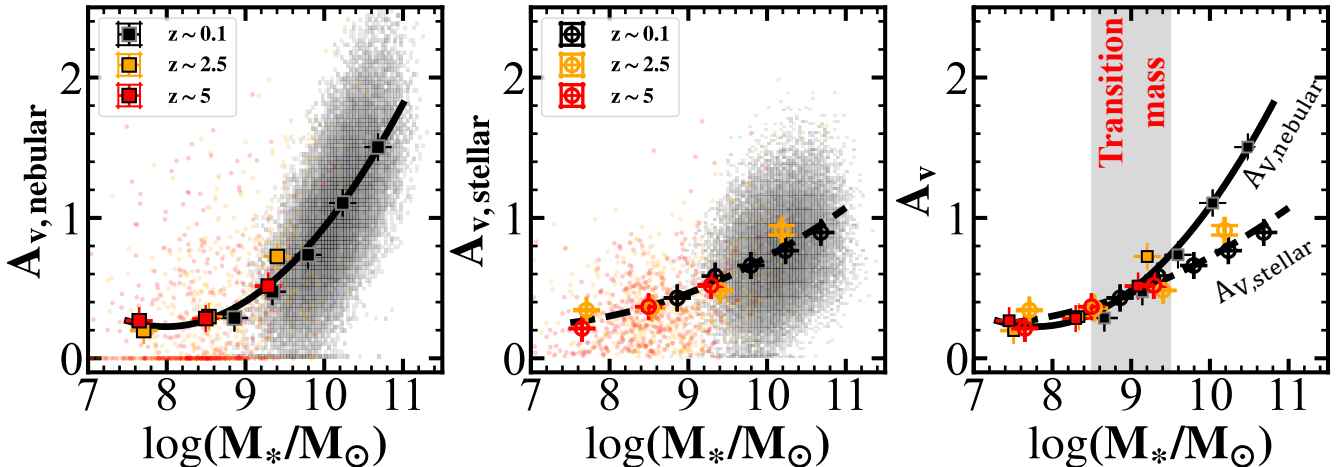


**Figure 4.** Dust attenuation as a function of  $M_*$ . The layout is similar to Figure 3. The left panel presents  $A_{V,\text{nebular}}$  versus  $M_*$ , while the middle panel shows  $A_{V,\text{stellar}}$  as a function of  $M_*$ . The filled squares and open circles represent the mean  $A_{V,\text{nebular}}$  and  $A_{V,\text{stellar}}$  values, respectively, calculated within different  $M_*$  bins. The error bars represent the standard error within each corresponding  $M_*$  bin. The corresponding best-fit relations derived in Section 4.3 are indicated by the black solid and dashed lines. For ease of comparison, the right panel displays both quantities side by side.

$z \sim 2.3$  from Shapley et al. (2022) are also overlaid as cyan diamonds.

Figure 3 shows that the BD increases monotonically with  $M_*$  across the entire redshift range, indicating that the correlation between the BD and  $M_*$  is already established at  $z \sim 7$ . Moreover, at fixed  $M_*$ , the BD values measured in different redshift bins are quite similar, demonstrating that  $M_*$  is the dominant parameter governing the BD. This result is in good agreement with previous findings (e.g., Shapley et al. 2023; Sandles et al. 2024; Woodrum et al. 2025). Furthermore, when we combine the samples across all redshift bins, evidence for a characteristic transition mass in this relation emerges. At  $\log(M_*/M_\odot) \lesssim 9$ , the BD rises only slowly with  $M_*$  and remains close to the theoretical Case B value, whereas at  $\log(M_*/M_\odot) \gtrsim 9$ , the BD increases more rapidly with  $M_*$ . This transition mass is marked by the shaded gray region in Figure 3.

Considering that the lack of redshift evolution of the BD– $M_*$  relation has been reported by many previous studies, we characterize the relation between  $M_*$  and the  $H\alpha/H\beta$  ratio using a single polynomial function for all redshift bins. To prevent the fit from being dominated by the SDSS sample, we performed a weighted least-squares fit to the mean values in each  $M_*$  bin. The resulting best-fit relation is

$$\begin{aligned} H\alpha/H\beta = & 0.26 \log(M_*/M_\odot)^2 \\ & - 4.25 \log(M_*/M_\odot) + 19.75, \end{aligned} \quad (4)$$

Additionally, we also investigated the mass dependence of each attenuation components. Figure 4 presents  $A_{V,\text{nebular}}$  (left panel) and  $A_{V,\text{stellar}}$  (middle panel) as functions of  $M_*$ , following a presentation similar to that of Figure 3, except that filled squares and open circles denote the mean values of  $A_{V,\text{nebular}}$  and  $A_{V,\text{stellar}}$  within each mass bin, respectively. As noted in Section 3.1, a subset of galaxies in our sample exhibit an observed  $H\alpha/H\beta$  ratio below the theoretical BD, which causes their inferred  $E(B-V)_{\text{nebular}}$  to be set to zero. We retain these galaxies in the following analysis because this behavior may reflect intrinsically low dust attenuation scattered below the theoretical floor by measurement uncertainty, as discussed in Section 3.1.

Across the full redshift range,  $A_{V,\text{nebular}}$  exhibits a clear positive correlation with  $M_*$ . Similar to the result of BD, we also see indications of a characteristic transition mass: above  $\log(M_*/M_\odot) \sim 9$ ,  $A_{V,\text{nebular}}$  rises rapidly with increasing  $M_*$ . This close parallel with the BD– $M_*$  relation is expected, since  $A_{V,\text{nebular}}$  is derived directly from the BD. The stellar attenuation  $A_{V,\text{stellar}}$  likewise correlates positively with  $M_*$  at all redshifts, but the rate of increase appears slower than

for  $A_{V,\text{nebular}}$ , and the evidence for a transition mass is correspondingly weaker. In addition, at fixed  $M_*$ , both  $A_{V,\text{nebular}}$  and  $A_{V,\text{stellar}}$  appear to remain constant with redshift. We will discuss the redshift evolution in more detail in Section 4.3.

To more directly assess whether  $A_{V,\text{nebular}}$  and  $A_{V,\text{stellar}}$  share the same dependence on  $M_*$ , the right panel of Figure 4 displays the two quantities side by side. For clarity of presentation, the  $A_{V,\text{nebular}}$  points are shifted leftward by 0.2 dex in  $\log(M_*/M_\odot)$  to avoid overlap with the  $A_{V,\text{stellar}}$  points. In this combined view, the evidence for a transition mass becomes more pronounced. At  $\log(M_*/M_\odot) \lesssim 9$ ,  $A_{V,\text{nebular}}$  and  $A_{V,\text{stellar}}$  are comparable in magnitude and exhibit similar dependences on  $M_*$ . However,  $A_{V,\text{nebular}}$  increases with  $M_*$  at a markedly faster rate than  $A_{V,\text{stellar}}$  above  $\log(M_*/M_\odot) \sim 9$ , so that  $A_{V,\text{nebular}}$  becomes systematically larger than  $A_{V,\text{stellar}}$  at the high-mass end.

## 4.2. Nebular-to-Stellar Attenuation Difference

### 4.2.1. Galaxies at $z \sim 0.1$

In the previous subsection, we examined how  $A_{V,\text{nebular}}$  and  $A_{V,\text{stellar}}$  depend on  $M_*$ . We now turn to their difference and investigate how it correlates with other galaxy physical properties. In this section, we consider both the difference in  $A_V$ , which is defined as:

$$A_{V,\text{diff}} \equiv A_{V,\text{nebular}} - A_{V,\text{stellar}} \quad (5)$$

and the ratio of  $E(B-V)$ . To avoid infinite values arising from setting  $E(B-V)_{\text{nebular}}$  to zero, we adopt the inverse of the conventional  $f$ -factor throughout the following sections, defining

$$\mathcal{R} \equiv E(B-V)_{\text{nebular}}/E(B-V)_{\text{stellar}} \quad (6)$$

Under this convention, the classic result of  $f = 0.44$  from Calzetti (1997) corresponds to  $\mathcal{R} = 2.27$ .

Figure 5 presents  $A_{V,\text{diff}}$  and  $\mathcal{R}$  as functions of  $M_*$  (left), SFR (middle), and sSFR (right) for our SDSS sample. The top row shows the results for  $A_{V,\text{diff}}$ , while the bottom row displays the corresponding trends for  $\mathcal{R}$ . Squares represent the values derived from the mean attenuation of the respective components in each bin of the relevant physical property, and the error bars indicate the  $1\sigma$  dispersion within each bin.

As shown in Figure 5, both  $A_{V,\text{diff}}$  and  $\mathcal{R}$  exhibit significant positive correlations with  $M_*$  and the SFR, while being anti-correlated with the sSFR. The quantity  $A_{V,\text{diff}}$  approaches 0 at  $\log(M_*/M_\odot) \sim 9$  and increases monotonically to nearly 1 mag at  $\log(M_*/M_\odot) \sim 11$ . Correspondingly,  $\mathcal{R}$  also increases monotonically from approximately 1 to the classic value of 2.27 observed in

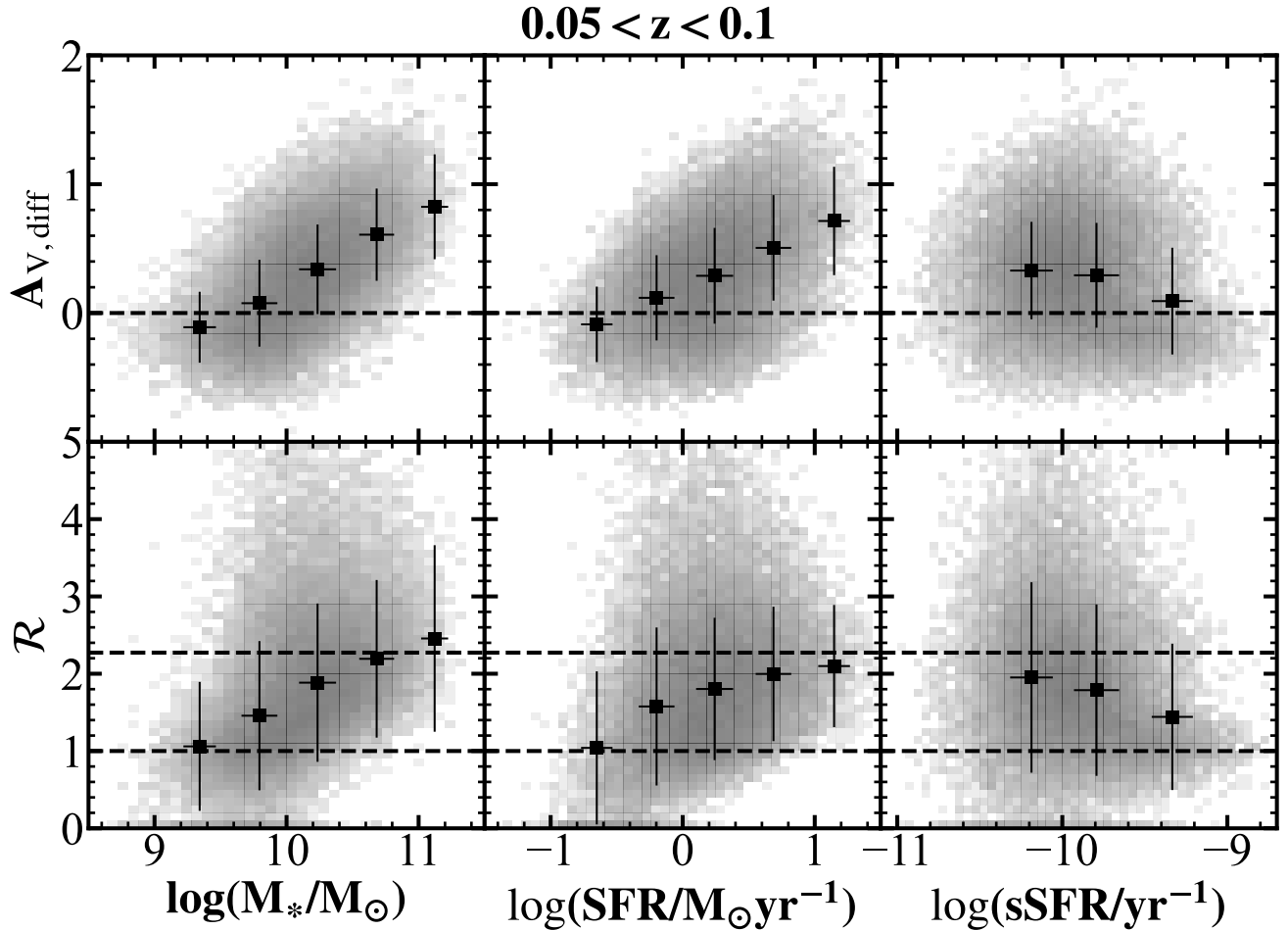


**Figure 5.** The difference in dust reddening between nebular and stellar components as a function of  $M_*$  (left column), SFR (middle column), and sSFR (right column). The top row shows the results of  $A_{V,\text{diff}}$ , while the bottom row presents the results of  $\mathcal{R}$ . Squares denote the values derived from the mean attenuation of the respective components in each bin of the relevant physical property, and the error bars show the corresponding  $1\sigma$  dispersion. For ease of comparison, we indicate  $A_{V,\text{diff}} = 0$  with a dashed line in the top panel. In the lower panel, dashed lines denote the unity ratio ( $\mathcal{R} = 1$ ) and the canonical value of  $\mathcal{R} = 2.27$  in the local universe.

**Table 3.** Spearman correlation results across different redshift bins

Redshift	Parameter	$\log(M_*/M_\odot)$		$\log(\text{SFR}/M_\odot\text{yr}^{-1})$		$\log(\text{sSFR}/\text{yr}^{-1})$	
		$r$	$p$	$r$	$p$	$r$	$p$
0.05 < z < 0.1	$A_{V,\text{diff}}$	0.568	< $10^{-5}$	0.422	< $10^{-5}$	-0.146	< $10^{-5}$
	$\mathcal{R}$	0.426	< $10^{-5}$	0.272	< $10^{-5}$	-0.158	< $10^{-5}$
1.5 < z < 3.5	$A_{V,\text{diff}}$	0.311	< $10^{-5}$	0.339	< $10^{-5}$	-0.134	0.003
	$\mathcal{R}$	0.373	< $10^{-5}$	0.413	< $10^{-5}$	-0.070	0.126
3.5 < z < 7	$A_{V,\text{diff}}$	-0.096	0.066	0.224	< $10^{-3}$	0.213	0.001
	$\mathcal{R}$	0.096	0.067	0.432	< $10^{-3}$	0.182	< $10^{-3}$

the local Universe over this mass range. These trends are mutually consistent, reflecting the underlying positive correlation between  $M_*$  and the SFR, as well as the inverse relationship between  $M_*$  and the sSFR. To quantify the significance of these relations, we computed the Spearman rank-order correlation coefficients for the full sample, as summarized in Table 3. In all cases, the associated  $p$ -values are below  $10^{-5}$ , indicating that the differential dust attenuation is statistically correlated with all three galaxy properties.

These results are broadly consistent with many prior studies of local star-forming galaxies (e.g., Wild et al. 2011; Battisti et al. 2016; Zahid et al. 2017; Koyama et al. 2019; Qin et al. 2019; Lin & Kong 2020; Li et al. 2021). For example, Zahid et al. (2017) derived  $A_{V,\text{stellar}}$  from stacked SDSS optical spectra and compared it to  $A_{V,\text{nebular}}$ , finding that the nebular-to-continuum attenuation ratio increases systematically with  $M_*$ . Similarly, Koyama et al. (2019) demonstrated that  $\mathcal{R}$  increases with  $M_*$ , approaching unity at the low-mass end. Numerous other studies have likewise reported a positive correlation between the differential attenuation and the SFR (e.g., Lin & Kong 2020; Li et al. 2021), in agreement with our findings. These findings are also consistent with the results presented in Figure 4. At the high-mass end,  $A_{V,\text{nebular}}$  increases more rapidly with  $M_*$  than  $A_{V,\text{stellar}}$ , producing an increasing difference between the two components as  $M_*$  increases.

#### 4.2.2. Galaxies at $z \sim 1.5 - 7$

Several studies have established that the  $\mathcal{R}$ -factor derived in the local universe is smaller than that observed in typical high-redshift star-forming galaxies. In this section, we utilize the JADES data to further investigate this issue. Following the approach described in Section 3.2, we divide our high-redshift sample into two redshift bins:  $1.5 < z < 3.5$  and  $3.5 < z < 7$ . The results for galaxies in these two redshift ranges are presented in Figures 6 and 7, respectively, in a format similar to that of Figure 5.

For the sample at  $z \sim 2.5$ , we find that the positive correlations of both  $A_{V,\text{diff}}$  and  $\mathcal{R}$  with  $M_*$  persist at high redshift, demonstrating that mass-dependent differential attenuation is not a phenomenon restricted to the local universe. Consistent with the local sample, both  $A_{V,\text{diff}}$  and  $\mathcal{R}$  exhibit positive correlations with the SFR, alongside a negative correlation with the sSFR. The corresponding Spearman rank-order correlation coefficients are summarized in Table 3. Notably, the JADES sample probes a lower characteristic  $M_*$  range ( $\log(M_*/M_\odot) \sim 7.5-10.5$ ) than the SDSS sample ( $\log(M_*/M_\odot) \sim 9-11.5$ ). Given the positive correlation

between  $A_{V,\text{diff}}$  and  $M_*$ , this lower characteristic mass naturally accounts for the median  $A_{V,\text{diff}}$  values that lie closer to zero at high redshift relative to the SDSS sample, without requiring genuine redshift evolution.

Prior to the JWST era, several studies had already investigated differential dust attenuation at  $z \sim 1-3$ , and our results are in good agreement with their findings. For instance, using 3D-HST spectroscopy, Price et al. (2014) reported that  $A_{V,\text{diff}}$  exhibits positive correlations with both  $M_*$  and SFR at  $z \sim 1.5$ . Similarly, Reddy et al. (2015) studied galaxies from the MOSDEF survey at  $1.4 < z < 2.6$  and reached the same conclusion. A number of other studies covering this epoch reported single-valued  $f$ -factor estimates without examining an explicit dependence on galaxy properties. For instance, Kashino et al. (2013) measured  $f \simeq 0.83$  at  $z \sim 1.6$ , while Theios et al. (2019) found an intermediate value of  $f \simeq 0.74$  at  $z \sim 2.0-2.7$ . Additionally, Pannella et al. (2015) obtained  $f \sim 1$  at  $z > 1.5$ , and Puglisi et al. (2016) reported  $f \sim 0.93$  at  $z \sim 1$ . These discrepancies are naturally understood when the different  $M_*$  ranges probed by these studies are taken into account: samples dominated by lower-mass galaxies preferentially yield  $f$  values closer to unity, whereas those with a higher characteristic mass tend to recover the canonical Calzetti (1997) value of  $f \approx 0.44$ .

Regarding the results at  $z \sim 5$ , we find no statistically significant correlation between  $A_{V,\text{diff}}$  (or  $\mathcal{R}$ ) and  $M_*$ , with the corresponding  $p$ -values of 0.066 and 0.067, respectively (as shown in Table 3). Furthermore, the median  $A_{V,\text{diff}}$  in this redshift bin is consistent with zero. This result likely reflects a combination of two sample-selection effects: the incompleteness of our sample at  $\log(M_*/M_\odot) < 8.5$  and the scarcity of massive galaxies ( $\log(M_*/M_\odot) > 10$ ) in the high-redshift JADES sample (Clarke et al. 2025). Nonetheless,  $A_{V,\text{diff}}$  retains a moderate positive correlation with the SFR ( $p < 0.05$ ). Similar results are also found over the redshift range  $1.5 < z < 3.5$ , where both  $A_{V,\text{diff}}$  and  $\mathcal{R}$  appear to exhibit stronger correlations with SFR, as shown in Table 3. However, as discussed in the Introduction, many previous studies have found that the relation between galaxy dust attenuation and  $M_*$  is redshift invariant. Therefore, here we mainly focus on the relation between  $A_{V,\text{diff}}$  and  $M_*$ . The physical quantity that exhibits the strongest correlation with  $A_{V,\text{diff}}$  will be investigated in more detail in future work.

Several other JWST-based studies have also examined differential dust attenuation at  $z > 3$ . Karthikeyan et al. (2026) analyzed a JADES sample of 283 star-forming galaxies at  $2.7 < z < 7$  and found a flat relation between  $E(B-V)_{\text{nebular}} - E(B-V)_{\text{stellar}}$  and  $M_*$  at  $z > 4$ , with

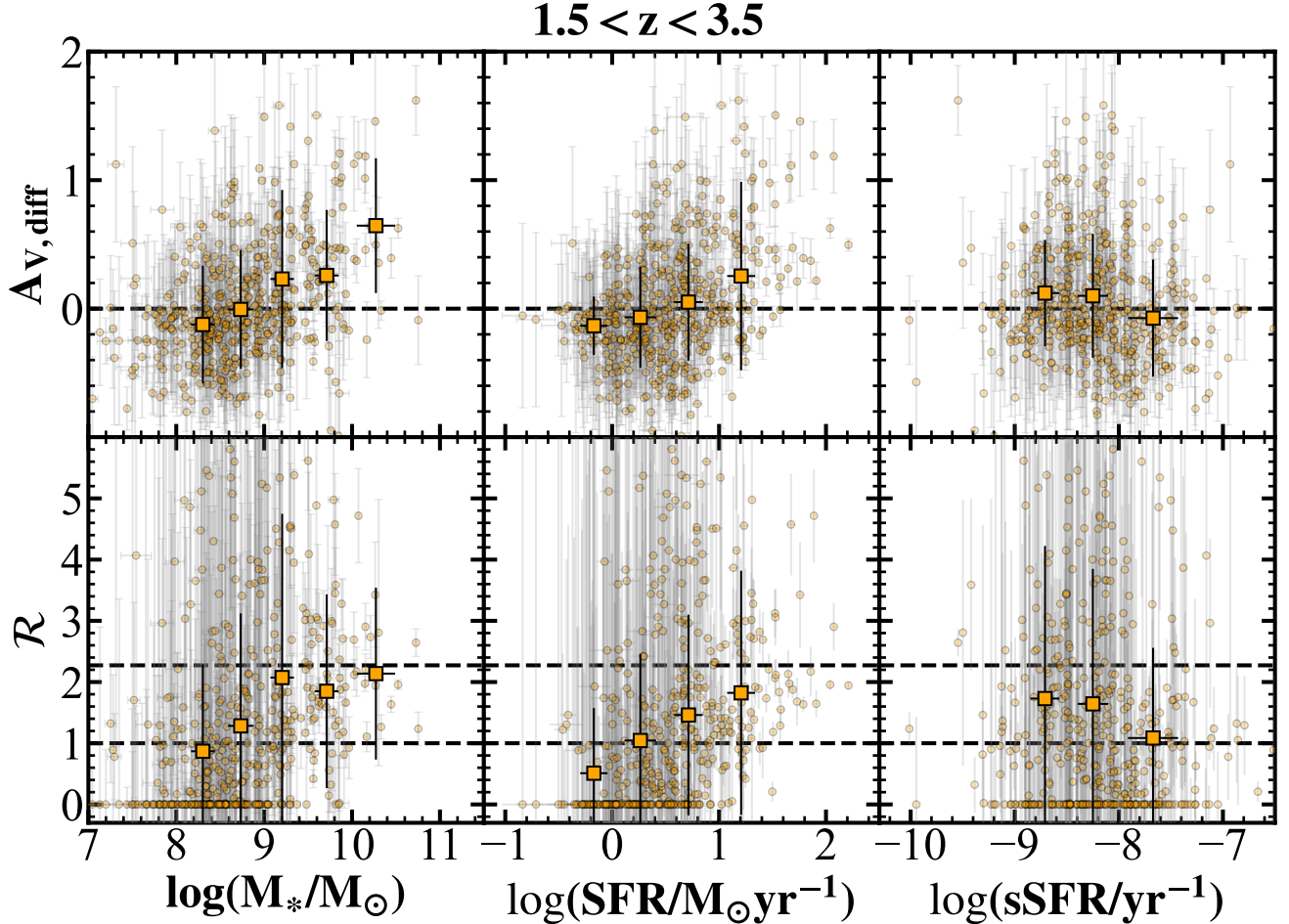


**Figure 6.** Similar to Figure 5, but showing the results for the sample at  $1.5 < z < 3.5$ . The background circles represent the measurements for individual galaxies. The squares denote the results in bins of each relevant physical property. The error bars indicate the  $1\sigma$  dispersion within the corresponding physical property bins.

values consistent with zero at  $z > 5$ , which is in good agreement with our results. In contrast, Woodrum et al. (2025) reported an unusually high mean ratio of  $\mathcal{R} \sim 14$  at  $z > 3$ . However, their analysis excluded galaxies with observed BD below 2.86, thereby preferentially removing low-attenuation systems from the sample. This selection criterion introduces a systematic bias toward elevated  $E(B - V)_{\text{nebular}}$  values, inflating the inferred  $\mathcal{R}$ . Additional JWST constraints from Tsujita et al. (2026) and Karthikeyan et al. (2026) report  $f$ -values in the range of  $\sim 0.5$ – $1.0$  at  $z \sim 3$ – $7$ , which are broadly consistent with our findings despite the significant uncertainties inherent in these measurements.

#### 4.3. Redshift Evolution

In the preceding subsections, we examined how  $A_{V,\text{nebular}}$ ,  $A_{V,\text{stellar}}$ , and their difference  $A_{V,\text{diff}}$  depend on  $M_*$ . In this section, we further examine the redshift evolution of these quantities. As discussed in Sections 4.1 and 4.2, investigating such evolution requires

comparison within a consistent  $M_*$  range. To this end, we select two mass bins,  $9.0 < \log(M_*/M_\odot) < 9.5$  and  $9.5 < \log(M_*/M_\odot) < 10.0$ , corresponding to the overlap region between the SDSS and JADES samples. The redshift evolution of  $A_{V,\text{nebular}}$ ,  $A_{V,\text{stellar}}$ , and  $A_{V,\text{diff}}$  within these two mass bins is presented in Figure 8. For clarity of presentation, results for the  $9.5 < \log(M_*/M_\odot) < 10.0$  bin are vertically offset by 0.75 mag, and the error bars indicate the  $1\sigma$  dispersion within each bin.

Figure 8 shows that, in both  $M_*$  bins,  $A_{V,\text{nebular}}$ ,  $A_{V,\text{stellar}}$ , and  $A_{V,\text{diff}}$  remain essentially unchanged with redshift, showing no statistically significant evolutionary trend. One exception is a slight elevation of  $A_{V,\text{nebular}}$  in the  $1.5 < z < 3.5$  bin. Correspondingly,  $A_{V,\text{diff}}$  is also slightly elevated over the same redshift range. This offset can be explained by our adoption of distinct Case B BD values for the two samples: 2.79 for the JADES sample and 2.86 for the SDSS sample (as discussed in Section 3.2), which propagates into a systematic differ-

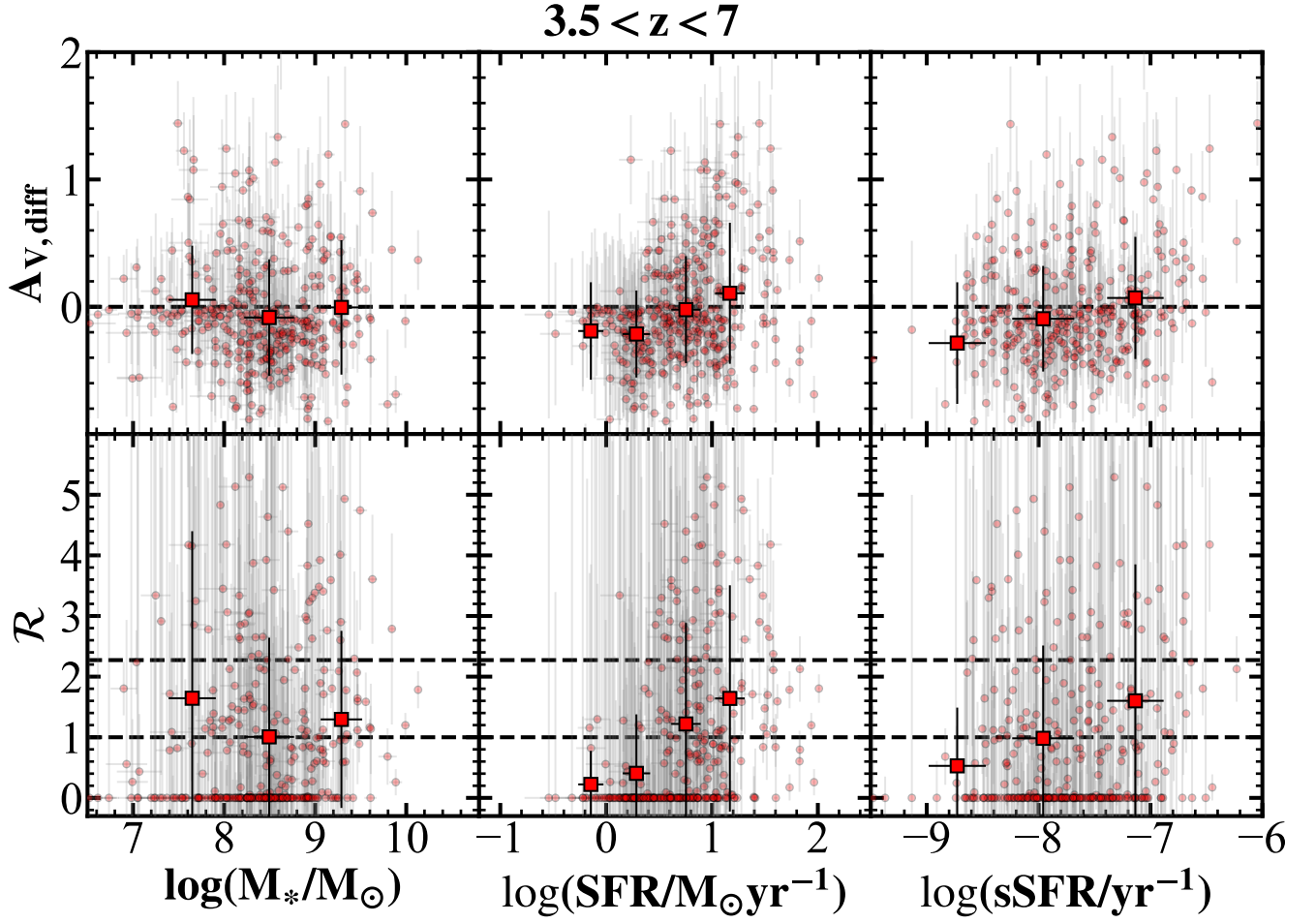


Figure 7. Similar to Figure 6, but showing the results for the sample at  $3.5 < z < 7$ .

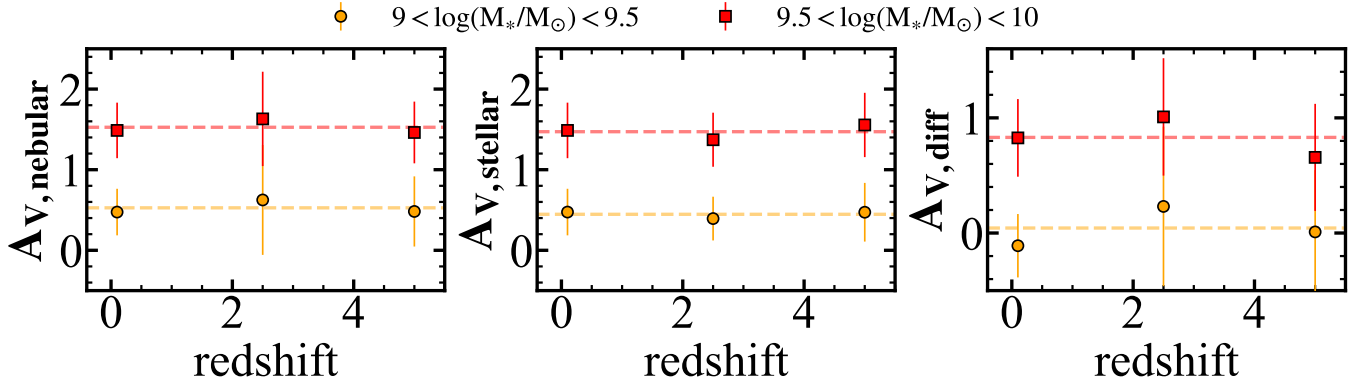
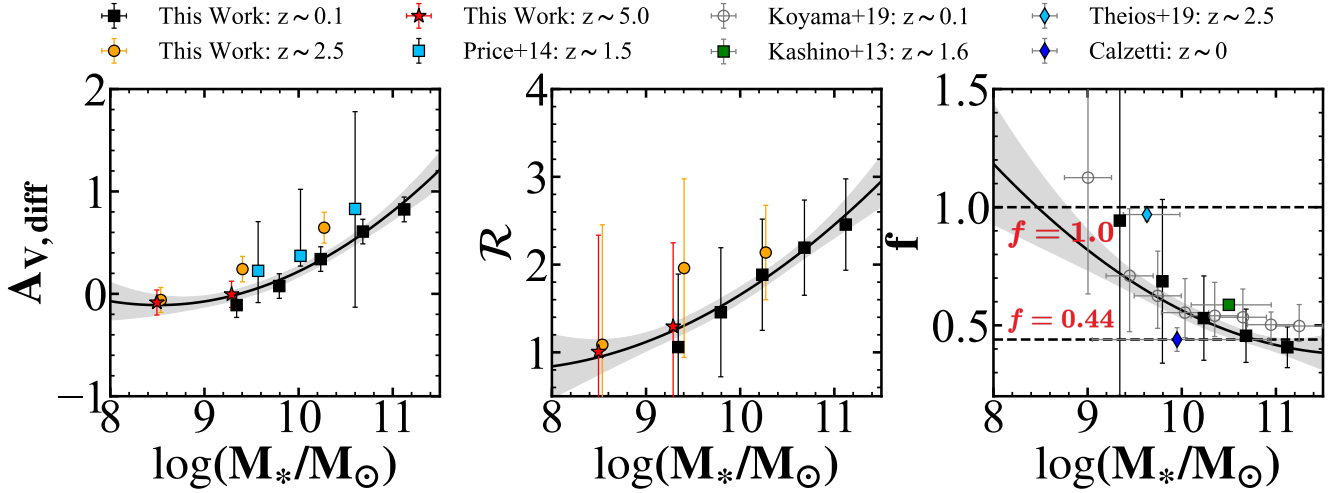
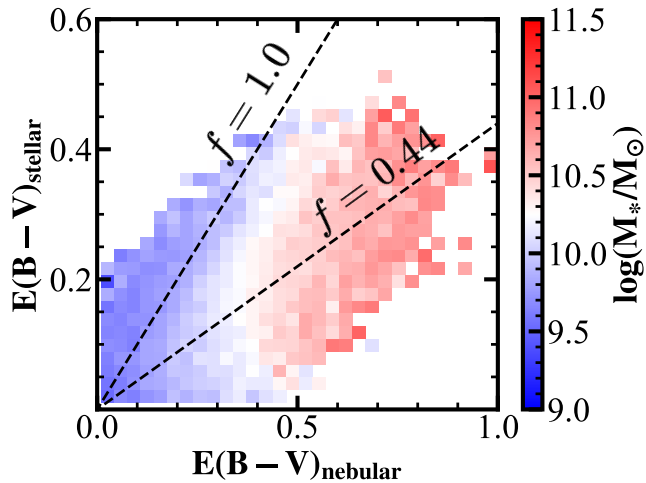


Figure 8. The redshift evolution of  $A_{V,nebular}$  (left),  $A_{V,stellar}$  (middle), and  $A_{V,diff}$  (right). The orange circles and red squares represent the result for galaxies with  $M_*$  in the ranges  $9 < \log(M_*/M_\odot) < 9.5$  and  $9.5 < \log(M_*/M_\odot) < 10$ , respectively. For clarity, the red squares are shifted upward by 0.75 mag.



**Figure 9.** The difference in dust reddening between nebular and stellar components as a function of  $M_*$  at different redshifts. The left panel presents the result of  $A_{V,diff}$  while the middle and right panel show the result of  $R$  and  $f$ , respectively. The black, orange, and red symbols correspond to the dust attenuation differences derived from the mean attenuation in each  $M_*$  bin for galaxies at  $0.05 < z < 0.1$ ,  $1.5 < z < 3.5$ , and  $3.5 < z < 7$ , respectively. The error bars are derived from the corresponding standard errors, with an additional 0.08 mag uncertainty in  $A_{V,nebular}$  caused by the choice of the intrinsic BD value. For clarity, we show only the  $z \sim 0.1$  results in the right panel; the  $z > 1.5$  results are omitted because they follow the same trend as in the middle panel. For ease of interpretation, we also indicate  $f = 0.44$  and  $1.0$  with dashed lines in the right panel. The best-fitting polynomial relation is shown as a black solid lines. The gray shaded region represents the uncertainty in the best-fitting result. For comparison, we also show the measurements from Calzetti (1997), Koyama et al. (2019), Kashino et al. (2013), Theios et al. (2019), and Price et al. (2014). Overall, our results are broadly consistent with previous studies. At fixed  $M_*$ , the reddening difference exhibits little to no significant evolution with redshift. When combining all redshift bins, the  $A_{V,diff}-M_*$  relation flattens at the low-mass end, while a positive correlation with  $M_*$  emerges at the high-mass end.



**Figure 10.** The comparison between  $E(B - V)_{\text{stellar}}$  and  $E(B - V)_{\text{nebular}}$ , where the color scale indicates the median  $M_*$  within each square bin. For reference, we also plot dashed lines corresponding to  $f = 0.44$ , and  $1.0$  in this figure. We find a clear trend in which more massive galaxies preferentially occupy the lower-right region of the diagram, indicating a smaller result of  $f$ .

ence of  $\sim 0.08$  mag in the inferred  $A_{V,\text{nebular}}$ , as inferred from Equations 2 and 3. Many earlier studies continued to assume the canonical intrinsic value of 2.86 at  $z < 3$ . If this standard intrinsic ratio were adopted for this redshift bin, the marginal elevation in  $A_{V,\text{nebular}}$  would vanish.

Moreover, adopting a single intrinsic BD value for all galaxies at  $z > 1.5$  remains a simplification. Since  $T_e$  scales with metallicity (which in turn correlates with stellar mass), using a mass-dependent intrinsic BD value would be more rigorous (e.g., Smith et al. 2022; Sandles et al. 2024). However, this is beyond the scope of this work. Given that the differences between  $1.5 < z < 3.5$  and the other redshift bins remain within the  $1\sigma$  dispersion, we conclude that, from  $z \sim 0.1$  to  $z \sim 7$ ,  $A_{V,\text{nebular}}$ ,  $A_{V,\text{stellar}}$ , and  $A_{V,\text{diff}}$  exhibit no significant redshift evolution at fixed  $M_*$  from  $z \sim 0.1$  to  $z \sim 7$ . However, we note that our sample lacks galaxies at  $0.1 \lesssim z \lesssim 1.5$ . In future work, we will use Subaru Prime Focus Spectrograph (Tamura et al. 2016) observation to obtain a more complete picture of the redshift evolution.

Given the absence of significant redshift evolution at fixed  $M_*$ , we can combine the low-redshift and high-redshift samples to characterize the global  $A_{V,\text{nebular}}-M_*$  and  $A_{V,\text{stellar}}-M_*$  relations across cosmic time. Following the approach used in Figure 3, we fit each relation with a polynomial function. The best-fit relations are overplotted as black solid and dashed lines for  $A_{V,\text{nebular}}$

and  $A_{V,\text{stellar}}$  in Figure 4, respectively. The best fitting relations are:

$$A_{V,\text{nebular}} = 0.17 \log(M_*/M_\odot)^2 - 2.79 \log(M_*/M_\odot) + 11.37 \quad (7)$$

$$A_{V,\text{stellar}} = 0.05 \log(M_*/M_\odot)^2 - 0.63 \log(M_*/M_\odot) + 2.36 \quad (8)$$

The potential redshift evolution of dust attenuation- $M_*$  relation has been a subject of long-standing debate. Numerous studies have demonstrated that the positive correlation between dust attenuation and  $M_*$  remains largely invariant from  $z \sim 0$  to  $z \sim 2$ . This stability has been observed in both  $A_{V,\text{nebular}}$  (e.g., Domínguez et al. 2013; Price et al. 2014; Shapley et al. 2022) and in  $A_{V,\text{stellar}}$  derived from SED fitting or infrared-to-UV star formation rate ratios (e.g., Meurer et al. 1999; Bouwens et al. 2016; Whitaker et al. 2017; McLure et al. 2018). Extending this to  $z > 3$ , recent *JWST* results suggest that the  $A_{V,\text{nebular}}-M_*$  relation continues to show no significant evolution (e.g., Shapley et al. 2023; Woodrum et al. 2025; Karthikeyan et al. 2026). The situation for  $A_{V,\text{stellar}}$ , however, remains less certain: while some investigations suggest no evolution out to  $z \sim 4$  (e.g., Pannella et al. 2015), others find a trend toward reduced attenuation at fixed  $M_*$  with increasing redshift (e.g., Fudamoto et al. 2020), and still others report that such a decrease is confined to the high-mass regime (e.g., Wijesekera et al. 2026). In this work, we find that the galaxy dust attenuation- $M_*$  relation exhibits no significant evolution out to  $z \sim 7$ . However, it should be noted that the  $M_*$  distributions of the SDSS and JADES samples differ substantially. Therefore, whether  $A_{V,\text{nebular}}$  and  $A_{V,\text{stellar}}$  evolve at fixed  $M_*$  over a broader  $M_*$  range still requires further investigation. In our sample, however, the high- and low-redshift galaxies lie on the same dust attenuation- $M_*$  sequence. More data are therefore needed to enable a more detailed analysis of the high-mass regime at high redshift.

Similarly, Figure 9 presents  $A_{V,\text{diff}}$  (left panel, defined in Equation 5) and  $\mathcal{R}$  (middle panel, defined in Equation 6) as functions of  $M_*$ , with the SDSS and JADES data from all redshift bins combined. Since previous studies have primarily focused on  $f$ , we also present the results for  $f$  (defined in Equation 1) in the right panel. However, for clarity, we show only the SDSS results in the right panel. To place our results within the broader context of the literature, we have also compiled measurements from Calzetti (1997), Kashino et al. (2013), Price et al. (2014), Koyama et al. (2019), and Theihs et al. (2019), which are overlaid on the figure for comparison. As illustrated in Figure 9, for  $A_{V,\text{diff}}$ , the SDSS

and JADES samples collapse onto a single continuous sequence, with no systematic offset between the low-redshift and high-redshift data at fixed  $M_*$ . A consistent trend is also observed for  $\mathcal{R}$  and  $f$ , although they exhibit substantially larger scatter. When compared with measurements from the literature, they fall on or very close to this combined sequence when evaluated at their corresponding  $M_*$ . The slight differences among results from different studies are expected, as they adopt different methodologies. This convergence of independent measurements supports the conclusion that  $M_*$ , rather than redshift, is the primary driver of the differential dust attenuation between the nebular and stellar components.

Combining the samples across all redshift bins reveals that the  $A_{V,\text{diff}}-M_*$  relation exhibits a characteristic two-regime behavior. At  $\log(M_*/M_\odot) \lesssim 9$ ,  $A_{V,\text{diff}}$  remains roughly constant near zero, indicating that the nebular and stellar components are subject to comparable levels of dust obscuration in low-mass galaxies. Above this threshold,  $A_{V,\text{diff}}$  rises monotonically with  $M_*$ , reaching  $\sim 1$  mag at  $\log(M_*/M_\odot) \sim 11$ . This behavior is fully consistent with the right panel of Figure 4: at the high-mass end,  $A_{V,\text{nebular}}$  increases more rapidly than  $A_{V,\text{stellar}}$ , naturally producing the monotonic rise of  $A_{V,\text{diff}}$  with  $M_*$ . To provide a quantitative description of this trend, we fit the  $A_{V,\text{diff}}-M_*$  relation with a polynomial function following the method used in Figure 3. The resulting best-fit relation is

$$A_{V,\text{diff}} = 0.15 \log(M_*/M_\odot)^2 - 2.51 \log(M_*/M_\odot) + 10.58 \quad (9)$$

which is shown as the black solid line in Figure 9.

The  $\mathcal{R}$  (and  $f$ ) factor exhibits a qualitatively similar behavior, remaining close to unity at low  $M_*$ , although with substantial scatter driven by the small absolute  $E(B-V)$  values in this regime, and increasing (decreasing) monotonically toward higher masses, ultimately approaching the canonical Calzetti (1997) value of  $\mathcal{R} = 2.27$  ( $f = 0.44$ ) at  $\log(M_*/M_\odot) \sim 11$ . We similarly fit the  $\mathcal{R}-M_*$  and  $f-M_*$  relation with a polynomial function. The resulting best-fit relation is

$$\mathcal{R} = 0.13 \log(M_*/M_\odot)^2 - 1.93 \log(M_*/M_\odot) + 7.96 \quad (10)$$

$$f = 0.05 \log(M_*/M_\odot)^2 - 1.29 \log(M_*/M_\odot) + 8.00 \quad (11)$$

which is overplotted as the black line in the middle and right panel of Figure 9.

Since many prior studies focused primarily on the  $f$  parameter, which exhibits substantial scatter in this

work, we provide a complementary perspective on the mass dependence of  $f$  in Figure 10. This figure illustrates the relationship between the two components through a two-dimensional histogram of  $E(B-V)_{\text{stellar}}$  versus  $E(B-V)_{\text{nebular}}$ . The color of each squares encodes the median  $M_*$  of galaxies within that bin. Because the JADES sample is small in comparison to the SDSS sample, only the SDSS galaxies are shown here. For reference, the loci corresponding to  $f = 1.0$  and  $0.44$  are overlaid as black dashed lines. As is evident from this figure, massive galaxies preferentially occupy the lower-right region of the plane, implying smaller  $f$  values for high-mass systems. This trend demonstrates that  $f$  is not a universal constant but is instead strongly coupled to the  $M_*$  of the host galaxy, in agreement with the trend revealed in Figure 9.

## 5. DISCUSSION

### 5.1. Results of different dust extinction curves

In this work, we investigated the dependence of  $A_{V,\text{nebular}}$ ,  $A_{V,\text{stellar}}$ , and their difference on  $M_*$ , as well as their possible redshift evolution. Compared with previous studies (e.g., Reddy et al. 2015; Koyama et al. 2019; Woodrum et al. 2025; Karthikeyan et al. 2026), our work covers a broader redshift range and focuses on the evolution at fixed stellar mass, revealing a universal extinction relation that does not evolve with redshift. In the preceding sections, we adopted a CAL attenuation curve for  $A_{V,\text{stellar}}$  and a MW extinction curve for  $A_{V,\text{nebular}}$  as our fiducial configuration. Although this choice was justified in Section 3.2, numerous studies have demonstrated that the effective dust attenuation curve varies considerably among individual galaxies (e.g., Salim et al. 2018; Fisher et al. 2025; Markov et al. 2025; Reddy et al. 2026). To assess the sensitivity of our findings to this assumption, we repeated the analysis using all nine pairwise combinations of three widely adopted curves: CAL, MW, and SMC.

Before presenting the results, we note that systematic offsets between different configurations are expected by construction. Because the three attenuation curves differ significantly in the UV range, where the SMC curve is the steepest and the CAL curve is the shallowest, the  $A_{V,\text{stellar}}$  inferred from SED fitting is expected to be smallest when the SMC curve is assumed and largest when the CAL curve is assumed. For the nebular component, Equations 2 and 3 represented in Section 3.2 imply  $A_{V,\text{nebular},\text{MW}} = 0.90 A_{V,\text{nebular},\text{CAL}} = 1.17 A_{V,\text{nebular},\text{SMC}}$ , indicating that the CAL curve yields the largest and the SMC curve the smallest  $A_{V,\text{nebular}}$  values. Consequently, different curve combinations produce systematic shifts in

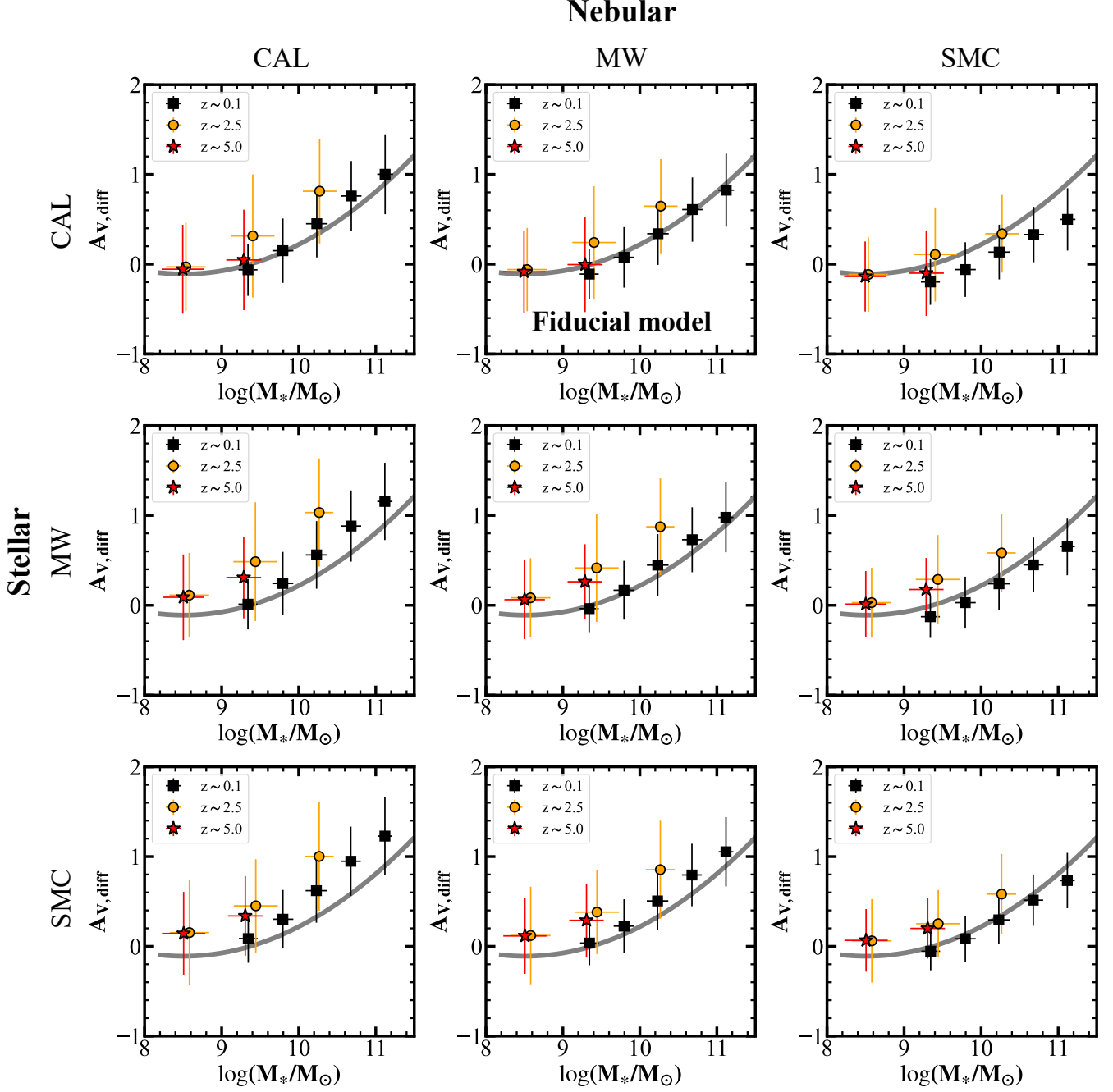


**Figure 11.** Similar to the left panel of Figure 9, but showing the results obtained using different dust attenuation curves. The error bars here represent the  $1\sigma$  dispersion. The gray solid line is the best-fit result for the Fiducial model described in Equation 9

the absolute normalization of  $A_{V,\text{diff}}$ . The relevant comparison for our analysis is therefore the relative trend with  $M_*$  rather than the absolute level.

Figure 11 presents the  $A_{V,\text{diff}}-M_*$  relation for all nine combinations, arranged in a  $3 \times 3$  grid in which rows correspond to the three assumed stellar attenuation curves and columns correspond to the three nebular extinction curves. For reference, the gray solid line in each panel

reproduces our fiducial best-fit relation from Figure 10. Although the absolute  $A_{V,\text{diff}}$  values shift systematically between panels in the manner described above, at fixed  $M_*$ , the median  $A_{V,\text{diff}}$  values across the three redshift bins remain consistent within the  $1\sigma$  dispersion in every configuration. A positive correlation between  $A_{V,\text{diff}}$  and  $M_*$  at the high-mass end is recovered under all nine configurations.

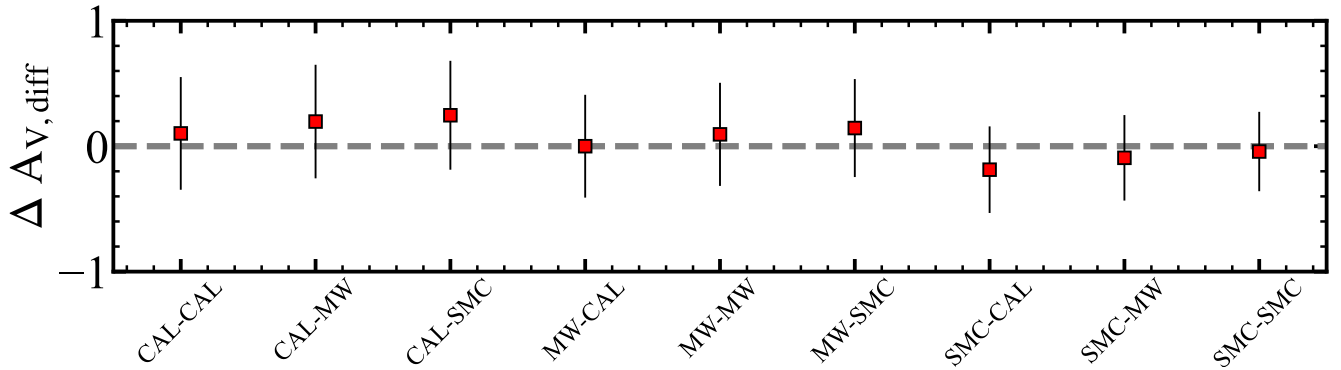


**Figure 12.** Average differences in  $A_{V,\text{diff}}$  for various dust attenuation curve configurations relative to our fiducial model (MW-CAL). The error bars represent the corresponding  $1\sigma$  dispersion. The horizontal axis indicates the specific combination of attenuation laws considered, denoted as the [nebular attenuation curve]–[stellar attenuation curve] combination.

To quantify these systematic shifts, we computed the mean difference in  $A_{V,\text{diff}}$  between each alternative configuration and our fiducial setup, as shown in Figure 12. The various combinations exhibit systematically positive or negative offsets that are entirely consistent with the expected differences in curve shapes. Notably, the absolute value of the mean offset remains within  $\sim 0.2$  mag for all nine pairings. This consistency confirms that the mass-dependent  $A_{V,\text{diff}}-M_*$  relation reported in Section 4 is not an artifact of our specific choice of attenuation curves but represents a robust feature of the data.

### 5.2. Physical Explanation

Through the analyses presented in Section 4, we have established a coherent observational framework. At fixed  $M_*$ , both  $A_{V,\text{stellar}}$  and  $A_{V,\text{nebular}}$  exhibit no significant evolution from  $z \sim 0.1$  to  $z \sim 7$ , and both correlate positively with  $M_*$ . These relations display a characteristic transition at  $\log(M_*/M_\odot) \sim 9$ : below this threshold, dust attenuation increases gradually with  $M_*$ , whereas above it, the slope steepens markedly. This steepening is more pronounced for  $A_{V,\text{nebular}}$  than for  $A_{V,\text{stellar}}$ , resulting in an  $A_{V,\text{diff}}$  that is consistent with zero at  $\log(M_*/M_\odot) \lesssim 9$  and increases monotonically toward higher masses. These features persist under all nine combinations of stellar and nebular attenuation curves tested in Section 5.1, indicating that they reflect intrinsic physical properties of the galaxy population rather than artifacts of methodological choices.

Because dust attenuation depends on the dust column density along each line of sight, it is governed jointly by the total dust content of a galaxy and its internal spatial distribution. The positive correlation between  $A_V$  and  $M_*$  follows naturally from the coupled mass–metallicity and mass–gas scaling relations (e.g., Tremonti et al. 2004; Maddox et al. 2015; Galliano et al. 2018; Li et al. 2019; Ding et al. 2023; Curti et al. 2023; Li et al. 2023, 2024; Kiyota et al. 2026): more massive galaxies host

higher gas-phase metallicities, facilitating more efficient grain growth and increasing the dust-to-gas ratio (e.g., Rémy-Ruyer et al. 2014). Simultaneously, the gas content also rises with  $M_*$  (e.g., Maddox et al. 2015), and these effects collectively lead to higher overall dust column densities in more massive systems.

The physical origin of the redshift invariance of dust attenuation at fixed  $M_*$  remains a subtle and active topic of debate. One widely discussed interpretation is that the effective dust column density scales primarily with  $M_*$  and is nearly independent of redshift (e.g., Whitaker et al. 2017; Shapley et al. 2022). Although prior studies have reported that the dust-to-stellar mass ratio in star-forming galaxies decreases with increasing redshift (e.g., Shivaeei et al. 2022; Jolly et al. 2025), several compensating effects may offset this decline. For instance, star-forming galaxies are systematically more compact at higher redshifts at the fixed stellar mass (e.g., Shibuya et al. 2015; Morishita et al. 2024; Song et al. 2025; Ceverino et al. 2026). Furthermore, some observations indicate that the dust-continuum sizes of high-redshift galaxies are even more concentrated than their rest-frame optical counterparts, suggesting a highly centrally concentrated dust distribution (e.g., Fujimoto et al. 2017; Popping et al. 2022). The resulting increase in dust surface density at fixed dust mass can partially counteract the reduction in the global dust-to-stellar mass ratio, thereby maintaining an effective line-of-sight column density that is approximately invariant over cosmic time. Additional factors, including a more clumpy dust geometry (e.g., Witt & Gordon 2000; Seon & Draine 2016), a non-unity dust covering fraction (e.g., Reddy et al. 2026), and the potential evolution of grain size distributions (e.g., Aoyama et al. 2020; Narayanan et al. 2023; Matsumoto et al. 2024; Parente et al. 2026; Matsumoto et al. 2026), may further modulate the integrated  $A_V$  at fixed total dust content. Disentangling these various contributions re-

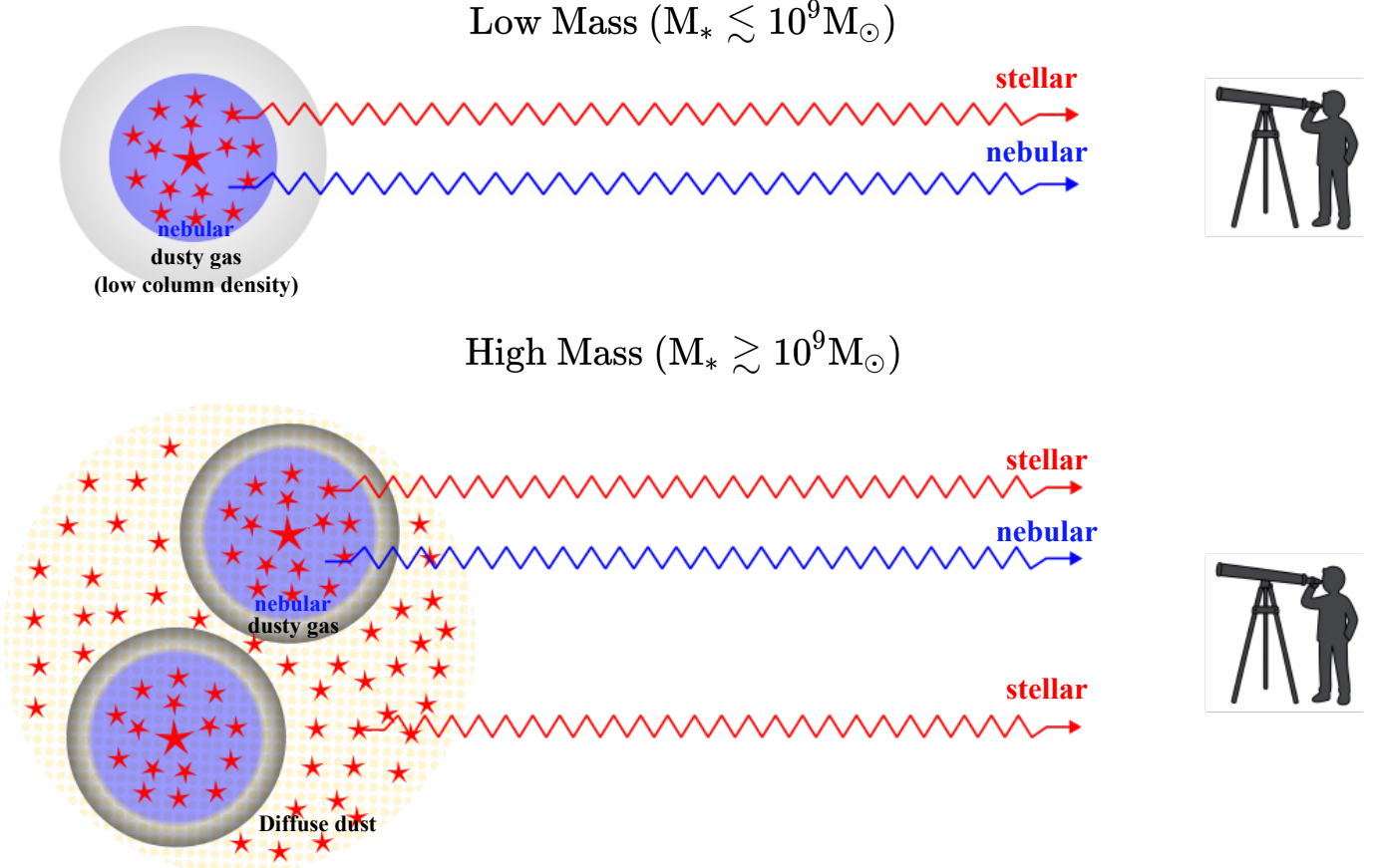


**Figure 13.** Schematic illustration of the two-component dust model for galaxies with low (top panel) and high (bottom panel)  $M_*$ . The gray region denotes birth cloud dust that has been dispersed by feedback processes. The light blue regions denote the nebular regions, while the light yellow regions represent the diffuse dust component within the ISM. Large red stars represent young, massive stars predominantly embedded within these birth clouds, whereas smaller red stars represent the less massive stellar populations. In low-mass galaxies, both the stellar continuum and nebular emission originate primarily from star-forming regions. Furthermore, due to the effects of stellar feedback, the birth clouds are blown apart and exhibit a more extended spatial distribution; consequently, the stellar and nebular light experience a similar degree of attenuation. In contrast, in high-mass galaxies, while nebular emission remains dominated by star-forming regions, a substantial fraction of the stellar continuum arises from older populations located outside the birth clouds. In these regions, the stellar light is primarily attenuated by the diffuse ISM. This geometric configuration leads to an increased discrepancy between  $A_{V,\text{nebular}}$  and  $A_{V,\text{stellar}}$  as a function of stellar mass.

quires higher-resolution multi-wavelength observations and is beyond the scope of the present work.

The transition near  $\log(M_*/M_\odot) \sim 9$ , above which  $A_{V,\text{nebular}}$  rises more steeply with stellar mass, may mark the mass scale where both the dust budget and the effective dust column density begin to increase nonlinearly. For high redshift galaxies, this mass is close to the point at which the mass–metallicity relation crosses the metallicity threshold for efficient dust growth: galaxies with  $M_* \sim 10^9 M_\odot$  typically reach  $12 + \log(\text{O}/\text{H}) \sim 8.2$ , corresponding to  $\sim 0.2\text{--}0.3 Z_\odot$  (e.g., Popping et al. 2017; Hirschmann et al. 2023; Kannan et al. 2025). This is comparable to the critical metallicity above which grain growth by accretion in the ISM becomes the dominant dust-production channel, leading to a rapid,

order-of-magnitude increase in  $M_{\text{dust}}/M_*$  or  $M_{\text{dust}}/M_{\text{gas}}$  (e.g., Asano et al. 2013a; Popping et al. 2017; Aoyama et al. 2018). Below this threshold, inefficient ISM grain growth, together with strong feedback in shallow gravitational potentials, prevents dust from building up efficiently in star-forming regions, so  $A_{V,\text{nebular}}$  varies only weakly with  $M_*$ . However, for low-redshift galaxies, the metallicity at  $M_* \sim 10^9 M_\odot$  is higher than  $0.5 Z_\odot$ , already exceeding the critical metallicity (e.g., Andrews & Martini 2013; Curti et al. 2020). Nevertheless, we find the same result at low redshift, suggesting that the critical metallicity alone may not be sufficient to explain our results.

Additionally, structural evolution may also affect the observed dust attenuation. Several cosmological simu-

lations indicate that, over the mass range around this threshold, galaxies with  $M_* \gtrsim 10^{8.5} M_\odot$  can enter a compact phase in which the stellar half-mass radius decreases with increasing  $M_*$  (e.g., Pillepich et al. 2018; Roper et al. 2022; Shen et al. 2024; Cataldi et al. 2026)<sup>15</sup>. This compaction is driven by high central gas densities and subsequent overcooling, which trigger centrally concentrated, bursty star formation (e.g., Roper et al. 2022; Cataldi et al. 2026). The resulting increase in gas and dust surface density enhances the column density toward H II regions, naturally producing the steeper rise of  $A_{V,\text{nebular}}$  above the observed transition mass.

The mass dependence of  $A_{V,\text{diff}}$  and  $\mathcal{R}$  admits a natural interpretation within the two-component dust framework. More specifically, it is set by the relative contributions of stellar continuum light from young and old populations, and is also shaped by the depth of the galaxy’s gravitational potential well. This physical picture is illustrated schematically in Figure 13.

Low-mass galaxies are characterized by higher sSFR (e.g., Tasca et al. 2015; Ceverino et al. 2018). As modeled by Kong et al. (2004), in such high-sSFR systems, the intense recent star formation ensures that young stars residing in nebular regions dominate the integrated continuum light. Because these components originate from spatially coincident regions, they probe similar dust column densities, naturally yielding  $A_{V,\text{nebular}} \approx A_{V,\text{stellar}}$ . A complementary effect operates in the same direction: feedback in low-mass galaxies repeatedly blows apart birth clouds (e.g., Li et al. 2026). This process broadens the effective spatial distribution of birth-cloud material, causing both young and older stars to sample a mixture of birth-cloud and diffuse-ISM attenuation, again yielding  $A_{V,\text{nebular}} \approx A_{V,\text{stellar}}$ .

In contrast, in massive galaxies, the older stellar populations that contribute substantially to the integrated continuum have migrated out of their natal clouds into the diffuse ISM. Furthermore, the deeper gravitational potentials allow birth clouds to persist longer and locate in the star-forming regions. This configuration results in the classical two-component geometry: nebular emission suffers from both diffuse-ISM and birth-cloud attenuation, whereas a significant fraction of the stellar continuum is attenuated only by the diffuse ISM, thereby producing  $A_{V,\text{nebular}} > A_{V,\text{stellar}}$  and  $\mathcal{R} > 1$ .

<sup>15</sup> In the simulations of Cataldi et al. (2026), the half-mass radius starts to increase again at  $M_* \gtrsim 10^{9.5} M_\odot$ , as normal inside-out growth is restored by continuous gas inflow; see also Furlong et al. (2017) and Lapiner et al. (2023)

## 6. SUMMARY

In this paper, we have presented a self-consistent census of nebular and stellar dust attenuation across cosmic time, utilizing a combined sample of 34,182 SDSS-GALEX star-forming galaxies at  $0.05 < z < 0.1$  and 863 *JWST*/JADES star-forming galaxies at  $1.5 < z < 7$ . Both samples were analyzed using a uniform BAGPIPES SED-fitting framework to derive  $A_{V,\text{stellar}}$ , complemented by Balmer-decrement-based  $A_{V,\text{nebular}}$  measurements. This homogenized treatment enables a direct comparison of the nebular-to-stellar dust attenuation across  $0 < z < 7$ . Our principal findings are summarized as follows:

(1) Both  $A_{V,\text{nebular}}$  and  $A_{V,\text{stellar}}$  correlate positively with  $M_*$  across all epochs. At a fixed  $M_*$ , both  $A_{V,\text{nebular}}$  and  $A_{V,\text{stellar}}$  exhibit no significant evolution with redshift from  $z \sim 7$  to  $z \sim 0$ , specifically, the mean dust attenuation values across the three redshift bins remain mutually consistent within the  $1\sigma$  scatter.

(2) Both the  $A_{V,\text{nebular}}-M_*$  and  $A_{V,\text{stellar}}-M_*$  relations exhibit a characteristic two-regime behavior, with a transition occurring near  $\log(M_*/M_\odot) \sim 9$ . Below this threshold, both attenuation components increase gradually with  $M_*$  and track each other closely. Above this mass, the relations steepen significantly. Additionally,  $A_{V,\text{nebular}}$  rises at a markedly higher rate than  $A_{V,\text{stellar}}$ , leading to an increasing divergence between the two components in massive galaxies.

(3) Differential attenuation  $A_{V,\text{diff}}$  correlates positively with  $M_*$  while exhibiting no statistically significant redshift evolution at a fixed  $M_*$ . At  $\log(M_*/M_\odot) \lesssim 9$ ,  $A_{V,\text{diff}}$  remains consistent with zero, indicating that the stellar and nebular components are subject to comparable levels of dust attenuation in low-mass galaxies. Above this threshold,  $A_{V,\text{diff}}$  rises monotonically with  $M_*$ , reaching  $\sim 1$  mag at  $\log(M_*/M_\odot) \sim 11$ . We demonstrate that this mass-dependent relation is robust within  $\sim \pm 0.2$  mag across all nine combinations of the assumed stellar and nebular attenuation curves (CAL, MW, and SMC).

Taken together, these results demonstrate that the longstanding  $f = 0.44$  value from Calzetti (1997) is not a universal constant, but is instead primarily determined by the  $M_*$  of the galaxy. This relation extends smoothly from  $f \sim 1$  at  $\log(M_*/M_\odot) \lesssim 9$  to  $f \sim 0.44$  at  $\log(M_*/M_\odot) \sim 11$ . The invariance of this relation from  $z \sim 7$  to  $z \sim 0$  suggests that the fundamental dust–star geometry underlying differential attenuation is established early in cosmic history and remains remarkably stable over the past 12 Gyr of galaxy evolution.

## ACKNOWLEDGMENTS

The authors thank Zesen Lin, Naveen A. Reddy, Hidenobu Yajima, and Hongxin Zhang for the valuable comments and discussions.

Funding for the Sloan Digital Sky Survey V has been provided by the Alfred P. Sloan Foundation, the Heising-Simons Foundation, the National Science Foundation, and the Participating Institutions. SDSS acknowledges support and resources from the Center for High-Performance Computing at the University of Utah. SDSS telescopes are located at Apache Point Observatory, funded by the Astrophysical Research Consortium and operated by New Mexico State University, and at Las Campanas Observatory, operated by the Carnegie Institution for Science. The SDSS web site is [www.sdss.org](http://www.sdss.org). SDSS is managed by the Astrophysical Research Consortium for the Participating Institutions of the SDSS Collaboration, including the Carnegie Institution for Science, Chilean National Time Allocation Committee (CNTAC) ratified researchers, Caltech, the Gotham Participation Group, Harvard University, Heidelberg University, The Flatiron Institute, The Johns Hopkins University, L’Ecole polytechnique fédérale de Lausanne (EPFL), Leibniz-Institut für Astrophysik Potsdam (AIP), Max-Planck-Institut für Astronomie (MPIA Heidelberg), Max-Planck-Institut für Extraterrestrische Physik (MPE), Nanjing University, National Astronomical Observatories of China (NAOC), New Mexico State University, The Ohio State University, Pennsylvania State University, Smithsonian Astrophysical Observatory, Space Telescope Science Institute (STScI), the Stellar Astrophysics Participation Group, Universidad Nacional Autónoma de México, University of Arizona, University of Colorado Boulder, University of Illinois at Urbana-Champaign, University of Toronto, University of Utah, University of Virginia, Yale University, and Yunnan University.

This research is based on observations made with the NASA Galaxy Evolution Explorer. GALEX is operated for NASA by the California Institute of Technology under NASA contract NAS5-98034.

This work is based on observations made with the NASA/ESA/CSA James Webb Space Telescope. The data were obtained from the Mikulski Archive for Space Telescopes at the Space Telescope Science Institute, which is operated by the Association of Universities for Research in Astronomy, Inc., under NASA contract NAS 5-03127 for JWST. The authors acknowledge the JADES (PIs: Daniel J. Eisenstein, Nora Luetzgendorf, and Kate Isaak) for developing their observing program with a zero-exclusive-access period. All the JWST data used in this paper can be found in MAST: <https://dx.doi.org/10.17909/8tdj-8n28>. The English writing in this paper has been improved with the help of ChatGPT, while the software does not generate sentences from scratch.

This work was supported by Outstanding Doctoral Students Overseas Study Program of the University of Science and Technology of China. This publication is based upon work supported by the World Premier International Research Center Initiative (WPI Initiative), MEXT, Japan, and KAKENHI (25H00674) through the Japan Society for the Promotion of Science. This work was supported by the joint research program of the Institute for Cosmic Ray Research (ICRR), University of Tokyo. T.K. was supported by JSPS KAKENHI Grant Number 26KJ1232. This work was supported by the National Natural Science Foundation of China (NSFC; Grant No. 12233008), the National Key R&D Program of China (No. 2023YFA1608100), and the Strategic Priority Research Program of the Chinese Academy of Sciences (No. XDB0550200). We also acknowledge support from the Cyrus Chun Ying Tang Foundation and the 111 Project for “Observational and Theoretical Research on Dark Matter and Dark Energy” (No. B23042). Y.N. acknowledges Flatiron Research Fellowship. The Flatiron Institute is a division of the Simons Foundation.

## REFERENCES

- Abazajian, K. N., Adelman-McCarthy, J. K., Agüeros, M. A., et al. 2009, *ApJS*, 182, 543, doi: [10.1088/0067-0049/182/2/543](https://doi.org/10.1088/0067-0049/182/2/543)
- Aihara, H., Allende Prieto, C., An, D., et al. 2011, *ApJS*, 193, 29, doi: [10.1088/0067-0049/193/2/29](https://doi.org/10.1088/0067-0049/193/2/29)
- Algera, H. S. B., Inami, H., Oesch, P. A., et al. 2023, *MNRAS*, 518, 6142, doi: [10.1093/mnras/stac3195](https://doi.org/10.1093/mnras/stac3195)
- Andrews, B. H., & Martini, P. 2013, *ApJ*, 765, 140, doi: [10.1088/0004-637X/765/2/140](https://doi.org/10.1088/0004-637X/765/2/140)
- Aoyama, S., Hirashita, H., & Nagamine, K. 2020, *MNRAS*, 491, 3844, doi: [10.1093/mnras/stz3253](https://doi.org/10.1093/mnras/stz3253)
- Aoyama, S., Hou, K.-C., Hirashita, H., Nagamine, K., & Shimizu, I. 2018, *MNRAS*, 478, 4905, doi: [10.1093/mnras/sty1431](https://doi.org/10.1093/mnras/sty1431)

- Aoyama, S., Hou, K.-C., Shimizu, I., et al. 2017, *MNRAS*, 466, 105, doi: [10.1093/mnras/stw3061](https://doi.org/10.1093/mnras/stw3061)
- Asano, R. S., Takeuchi, T. T., Hirashita, H., & Inoue, A. K. 2013a, *Earth, Planets and Space*, 65, 213, doi: [10.5047/eps.2012.04.014](https://doi.org/10.5047/eps.2012.04.014)
- Asano, R. S., Takeuchi, T. T., Hirashita, H., & Nozawa, T. 2013b, *MNRAS*, 432, 637, doi: [10.1093/mnras/stt506](https://doi.org/10.1093/mnras/stt506)
- Bakx, T. J. L. C. 2026, arXiv e-prints, arXiv:2604.01089, doi: [10.48550/arXiv.2604.01089](https://doi.org/10.48550/arXiv.2604.01089)
- Baldwin, J. A., Phillips, M. M., & Terlevich, R. 1981, *PASP*, 93, 5, doi: [10.1086/130766](https://doi.org/10.1086/130766)
- Battisti, A. J., Calzetti, D., & Chary, R.-R. 2016, *ApJ*, 818, 13, doi: [10.3847/0004-637X/818/1/13](https://doi.org/10.3847/0004-637X/818/1/13)
- . 2017, *ApJ*, 851, 90, doi: [10.3847/1538-4357/aa9a43](https://doi.org/10.3847/1538-4357/aa9a43)
- Böker, T., Beck, T. L., Birkmann, S. M., et al. 2023, *PASP*, 135, 038001, doi: [10.1088/1538-3873/acb846](https://doi.org/10.1088/1538-3873/acb846)
- Bouwens, R. J., Aravena, M., Decarli, R., et al. 2016, *ApJ*, 833, 72, doi: [10.3847/1538-4357/833/1/72](https://doi.org/10.3847/1538-4357/833/1/72)
- Brinchmann, J., Charlot, S., White, S. D. M., et al. 2004, *MNRAS*, 351, 1151, doi: [10.1111/j.1365-2966.2004.07881.x](https://doi.org/10.1111/j.1365-2966.2004.07881.x)
- Budavári, T., Heinis, S., Szalay, A. S., et al. 2009, *ApJ*, 694, 1281, doi: [10.1088/0004-637X/694/2/1281](https://doi.org/10.1088/0004-637X/694/2/1281)
- Bunker, A. J., Cameron, A. J., Curtis-Lake, E., et al. 2024, *A&A*, 690, A288, doi: [10.1051/0004-6361/202347094](https://doi.org/10.1051/0004-6361/202347094)
- Calzetti, D. 1997, *AJ*, 113, 162, doi: [10.1086/118242](https://doi.org/10.1086/118242)
- Calzetti, D., Armus, L., Bohlin, R. C., et al. 2000, *ApJ*, 533, 682, doi: [10.1086/308692](https://doi.org/10.1086/308692)
- Calzetti, D., Kinney, A. L., & Storchi-Bergmann, T. 1994, *ApJ*, 429, 582, doi: [10.1086/174346](https://doi.org/10.1086/174346)
- Cameron, A. J., Katz, H., Witten, C., et al. 2024, *MNRAS*, 534, 523, doi: [10.1093/mnras/stae1547](https://doi.org/10.1093/mnras/stae1547)
- Cardelli, J. A., Clayton, G. C., & Mathis, J. S. 1989, *ApJ*, 345, 245, doi: [10.1086/167900](https://doi.org/10.1086/167900)
- Carnall, A. C., McLure, R. J., Dunlop, J. S., & Davé, R. 2018, *MNRAS*, 480, 4379, doi: [10.1093/mnras/sty2169](https://doi.org/10.1093/mnras/sty2169)
- Carnall, A. C., McLure, R. J., Dunlop, J. S., et al. 2019, *MNRAS*, 490, 417, doi: [10.1093/mnras/stz2544](https://doi.org/10.1093/mnras/stz2544)
- Cataldi, P., Pedrosa, S., Pellizza, L. J., Ceverino, D., & Bignone, L. A. 2026, *A&A*, 706, A125, doi: [10.1051/0004-6361/202556078](https://doi.org/10.1051/0004-6361/202556078)
- Ceverino, D., Klessen, R. S., & Glover, S. C. O. 2018, *MNRAS*, 480, 4842, doi: [10.1093/mnras/sty2124](https://doi.org/10.1093/mnras/sty2124)
- Ceverino, D., Nakazato, Y., Yoshida, N., et al. 2026, arXiv e-prints, arXiv:2603.05045, doi: [10.48550/arXiv.2603.05045](https://doi.org/10.48550/arXiv.2603.05045)
- Charlot, S., & Fall, S. M. 2000, *ApJ*, 539, 718, doi: [10.1086/309250](https://doi.org/10.1086/309250)
- Chevallard, J., Charlot, S., Wandelt, B., & Wild, V. 2013, *MNRAS*, 432, 2061, doi: [10.1093/mnras/stt523](https://doi.org/10.1093/mnras/stt523)
- Clarke, L., Shapley, A. E., Lam, N., et al. 2025, arXiv e-prints, arXiv:2510.06681, doi: [10.48550/arXiv.2510.06681](https://doi.org/10.48550/arXiv.2510.06681)
- Clarke, L., Shapley, A. E., Sanders, R. L., et al. 2024, *ApJ*, 977, 133, doi: [10.3847/1538-4357/ad8ba4](https://doi.org/10.3847/1538-4357/ad8ba4)
- Curti, M., Mannucci, F., Cresci, G., & Maiolino, R. 2020, *MNRAS*, 491, 944, doi: [10.1093/mnras/stz2910](https://doi.org/10.1093/mnras/stz2910)
- Curti, M., D'Eugenio, F., Carniani, S., et al. 2023, *MNRAS*, 518, 425, doi: [10.1093/mnras/stac2737](https://doi.org/10.1093/mnras/stac2737)
- Curtis-Lake, E., Cameron, A. J., Bunker, A. J., et al. 2025, arXiv e-prints, arXiv:2510.01033, doi: [10.48550/arXiv.2510.01033](https://doi.org/10.48550/arXiv.2510.01033)
- D'Eugenio, F., Cameron, A. J., Scholtz, J., et al. 2025, *ApJS*, 277, 4, doi: [10.3847/1538-4365/ada148](https://doi.org/10.3847/1538-4365/ada148)
- Ding, W., Zou, H., Kong, X., et al. 2023, *AJ*, 166, 133, doi: [10.3847/1538-3881/ace893](https://doi.org/10.3847/1538-3881/ace893)
- Dole, H., Lagache, G., Puget, J.-L., et al. 2006, *A&A*, 451, 417, doi: [10.1051/0004-6361:20054446](https://doi.org/10.1051/0004-6361:20054446)
- Domínguez, A., Siana, B., Henry, A. L., et al. 2013, *ApJ*, 763, 145, doi: [10.1088/0004-637X/763/2/145](https://doi.org/10.1088/0004-637X/763/2/145)
- Draine, B. T. 2011, *Physics of the Interstellar and Intergalactic Medium*
- Eisenstein, D. J., Willott, C., Alberts, S., et al. 2023, arXiv e-prints, arXiv:2306.02465, doi: [10.48550/arXiv.2306.02465](https://doi.org/10.48550/arXiv.2306.02465)
- Eisenstein, D. J., Johnson, B. D., Robertson, B., et al. 2025, *ApJS*, 281, 50, doi: [10.3847/1538-4365/ae1137](https://doi.org/10.3847/1538-4365/ae1137)
- Ferruit, P., Jakobsen, P., Giardino, G., et al. 2022, *A&A*, 661, A81, doi: [10.1051/0004-6361/202142673](https://doi.org/10.1051/0004-6361/202142673)
- Fisher, R., Bowler, R. A. A., Stefanon, M., et al. 2025, *MNRAS*, 539, 109, doi: [10.1093/mnras/staf485](https://doi.org/10.1093/mnras/staf485)
- Fudamoto, Y., Oesch, P. A., Magnelli, B., et al. 2020, *MNRAS*, 491, 4724, doi: [10.1093/mnras/stz3248](https://doi.org/10.1093/mnras/stz3248)
- Fujimoto, S., Ouchi, M., Shibuya, T., & Nagai, H. 2017, *ApJ*, 850, 83, doi: [10.3847/1538-4357/aa93e6](https://doi.org/10.3847/1538-4357/aa93e6)
- Furlong, M., Bower, R. G., Crain, R. A., et al. 2017, *MNRAS*, 465, 722, doi: [10.1093/mnras/stw2740](https://doi.org/10.1093/mnras/stw2740)
- Galliano, F., Galametz, M., & Jones, A. P. 2018, *ARA&A*, 56, 673, doi: [10.1146/annurev-astro-081817-051900](https://doi.org/10.1146/annurev-astro-081817-051900)
- Garn, T., & Best, P. N. 2010, *MNRAS*, 409, 421, doi: [10.1111/j.1365-2966.2010.17321.x](https://doi.org/10.1111/j.1365-2966.2010.17321.x)
- Gordon, K. D., Clayton, G. C., Misselt, K. A., Landolt, A. U., & Wolff, M. J. 2003, *ApJ*, 594, 279, doi: [10.1086/376774](https://doi.org/10.1086/376774)
- Hainline, K. N., Johnson, B. D., Robertson, B., et al. 2024, *ApJ*, 964, 71, doi: [10.3847/1538-4357/ad1ee4](https://doi.org/10.3847/1538-4357/ad1ee4)
- Heintz, K. E., Brammer, G. B., Watson, D., et al. 2025, *A&A*, 693, A60, doi: [10.1051/0004-6361/202450243](https://doi.org/10.1051/0004-6361/202450243)
- Hirschmann, M., Charlot, S., Feltre, A., et al. 2023, *MNRAS*, 526, 3610, doi: [10.1093/mnras/stad2955](https://doi.org/10.1093/mnras/stad2955)

- Jakobsen, P., Ferruit, P., Alves de Oliveira, C., et al. 2022, *A&A*, 661, A80, doi: [10.1051/0004-6361/202142663](https://doi.org/10.1051/0004-6361/202142663)
- Jolly, J.-B., Knudsen, K., Laporte, N., et al. 2025, *A&A*, 693, A190, doi: [10.1051/0004-6361/202346239](https://doi.org/10.1051/0004-6361/202346239)
- Juodžbalis, I., Maiolino, R., Baker, W. M., et al. 2025, arXiv e-prints, arXiv:2504.03551, doi: [10.48550/arXiv.2504.03551](https://doi.org/10.48550/arXiv.2504.03551)
- Kannan, R., Puchwein, E., Smith, A., et al. 2025, *The Open Journal of Astrophysics*, 8, 153, doi: [10.33232/001c.145804](https://doi.org/10.33232/001c.145804)
- Karthikeyan, S., Clarke, L., Shapley, A. E., et al. 2026, arXiv e-prints, arXiv:2603.11338, doi: [10.48550/arXiv.2603.11338](https://doi.org/10.48550/arXiv.2603.11338)
- Kashino, D., Silverman, J. D., Rodighiero, G., et al. 2013, *ApJL*, 777, L8, doi: [10.1088/2041-8205/777/1/L8](https://doi.org/10.1088/2041-8205/777/1/L8)
- Kauffmann, G., Heckman, T. M., White, S. D. M., et al. 2003a, *MNRAS*, 341, 33, doi: [10.1046/j.1365-8711.2003.06291.x](https://doi.org/10.1046/j.1365-8711.2003.06291.x)
- Kauffmann, G., Heckman, T. M., Tremonti, C., et al. 2003b, *MNRAS*, 346, 1055, doi: [10.1111/j.1365-2966.2003.07154.x](https://doi.org/10.1111/j.1365-2966.2003.07154.x)
- Kennicutt, R. C., & Evans, N. J. 2012, *ARA&A*, 50, 531, doi: [10.1146/annurev-astro-081811-125610](https://doi.org/10.1146/annurev-astro-081811-125610)
- Kennicutt, Jr., R. C. 1998, *ARA&A*, 36, 189, doi: [10.1146/annurev.astro.36.1.189](https://doi.org/10.1146/annurev.astro.36.1.189)
- Kewley, L. J., Jansen, R. A., & Geller, M. J. 2005, *PASP*, 117, 227, doi: [10.1086/428303](https://doi.org/10.1086/428303)
- Kiyota, T., Ouchi, M., Iono, D., et al. 2026, arXiv e-prints, arXiv:2601.18149, doi: [10.48550/arXiv.2601.18149](https://doi.org/10.48550/arXiv.2601.18149)
- Kong, X., Charlot, S., Brinchmann, J., & Fall, S. M. 2004, *MNRAS*, 349, 769, doi: [10.1111/j.1365-2966.2004.07556.x](https://doi.org/10.1111/j.1365-2966.2004.07556.x)
- Koyama, Y., Shimakawa, R., Yamamura, I., Kodama, T., & Hayashi, M. 2019, *PASJ*, 71, 8, doi: [10.1093/pasj/psy113](https://doi.org/10.1093/pasj/psy113)
- Kroupa, P. 2001, *MNRAS*, 322, 231, doi: [10.1046/j.1365-8711.2001.04022.x](https://doi.org/10.1046/j.1365-8711.2001.04022.x)
- Lapiner, S., Dekel, A., Freundlich, J., et al. 2023, *MNRAS*, 522, 4515, doi: [10.1093/mnras/stad1263](https://doi.org/10.1093/mnras/stad1263)
- Leja, J., Carnall, A. C., Johnson, B. D., Conroy, C., & Speagle, J. S. 2019, *ApJ*, 876, 3, doi: [10.3847/1538-4357/ab133c](https://doi.org/10.3847/1538-4357/ab133c)
- Li, F., Wang, J., Xu, F., et al. 2023, *ApJ*, 950, 84, doi: [10.3847/1538-4357/acbc0](https://doi.org/10.3847/1538-4357/acbc0)
- Li, F., Wang, E., Zhu, M., et al. 2024, *ApJ*, 974, 238, doi: [10.3847/1538-4357/ad6b97](https://doi.org/10.3847/1538-4357/ad6b97)
- Li, F., Zhang, H.-X., Brinks, E., et al. 2026, *A&A*, 708, A233, doi: [10.1051/0004-6361/202557482](https://doi.org/10.1051/0004-6361/202557482)
- Li, N., Li, C., Mo, H., et al. 2021, *ApJ*, 917, 72, doi: [10.3847/1538-4357/ac0973](https://doi.org/10.3847/1538-4357/ac0973)
- Li, Q., Narayanan, D., & Davé, R. 2019, *MNRAS*, 490, 1425, doi: [10.1093/mnras/stz2684](https://doi.org/10.1093/mnras/stz2684)
- Lin, Z., & Kong, X. 2020, *ApJ*, 888, 88, doi: [10.3847/1538-4357/ab5f0e](https://doi.org/10.3847/1538-4357/ab5f0e)
- Lin, Z., & Yan, R. 2024, *A&A*, 691, A201, doi: [10.1051/0004-6361/202451339](https://doi.org/10.1051/0004-6361/202451339)
- López Fernández, R., Cid Fernandes, R., González Delgado, R. M., et al. 2016, *MNRAS*, 458, 184, doi: [10.1093/mnras/stw260](https://doi.org/10.1093/mnras/stw260)
- Lorenz, B., Suess, K. A., Kriek, M., et al. 2025, *ApJL*, 988, L20, doi: [10.3847/2041-8213/ade887](https://doi.org/10.3847/2041-8213/ade887)
- Lyu, J., Alberts, S., Rieke, G. H., & Rujopakarn, W. 2022, *ApJ*, 941, 191, doi: [10.3847/1538-4357/ac9e5d](https://doi.org/10.3847/1538-4357/ac9e5d)
- Maddox, N., Hess, K. M., Obreschkow, D., Jarvis, M. J., & Blyth, S.-L. 2015, *MNRAS*, 447, 1610, doi: [10.1093/mnras/stu2532](https://doi.org/10.1093/mnras/stu2532)
- Markov, V., Gallerani, S., Ferrara, A., et al. 2025, *Nature Astronomy*, 9, 458, doi: [10.1038/s41550-024-02426-1](https://doi.org/10.1038/s41550-024-02426-1)
- Martin, D. C., Fanson, J., Schiminovich, D., et al. 2005, *ApJL*, 619, L1, doi: [10.1086/426387](https://doi.org/10.1086/426387)
- Martin, D. C., Wyder, T. K., Schiminovich, D., et al. 2007, *ApJS*, 173, 342, doi: [10.1086/516639](https://doi.org/10.1086/516639)
- Mathis, J. S., Rumpl, W., & Nordsieck, K. H. 1977, *ApJ*, 217, 425, doi: [10.1086/155591](https://doi.org/10.1086/155591)
- Matsumoto, K., Hirashita, H., Nagamine, K., et al. 2024, *A&A*, 689, A79, doi: [10.1051/0004-6361/202449454](https://doi.org/10.1051/0004-6361/202449454)
- Matsumoto, K., Sommovigo, L., Gebek, A., et al. 2026, *A&A*, 705, A75, doi: [10.1051/0004-6361/202555658](https://doi.org/10.1051/0004-6361/202555658)
- McClymont, W., Tacchella, S., D'Eugenio, F., et al. 2025, *MNRAS*, 540, 190, doi: [10.1093/mnras/staf745](https://doi.org/10.1093/mnras/staf745)
- McLure, R. J., Dunlop, J. S., Cullen, F., et al. 2018, *MNRAS*, 476, 3991, doi: [10.1093/mnras/sty522](https://doi.org/10.1093/mnras/sty522)
- Mehta, V., Teplitz, H. I., Scarlata, C., et al. 2023, *ApJ*, 952, 133, doi: [10.3847/1538-4357/acd9cf](https://doi.org/10.3847/1538-4357/acd9cf)
- Meurer, G. R., Heckman, T. M., & Calzetti, D. 1999, *ApJ*, 521, 64, doi: [10.1086/307523](https://doi.org/10.1086/307523)
- Morishita, T., Stiavelli, M., Chary, R.-R., et al. 2024, *ApJ*, 963, 9, doi: [10.3847/1538-4357/ad1404](https://doi.org/10.3847/1538-4357/ad1404)
- Nakazato, Y., Matsumoto, K., Inoue, A. K., et al. 2026, arXiv e-prints, arXiv:2602.07347, doi: [10.48550/arXiv.2602.07347](https://doi.org/10.48550/arXiv.2602.07347)
- Narayanan, D., Conroy, C., Davé, R., Johnson, B. D., & Popping, G. 2018, *ApJ*, 869, 70, doi: [10.3847/1538-4357/aaed25](https://doi.org/10.3847/1538-4357/aaed25)
- Narayanan, D., Smith, J.-D. T., Hensley, B. S., et al. 2023, *ApJ*, 951, 100, doi: [10.3847/1538-4357/accf8d](https://doi.org/10.3847/1538-4357/accf8d)
- O'Donnell, J. E. 1994, *ApJ*, 422, 158, doi: [10.1086/173713](https://doi.org/10.1086/173713)
- Osterbrock, D. E. 1989, *Astrophysics of gaseous nebulae and active galactic nuclei*
- Oteo, I., Bongiovanni, Á., Magdis, G., et al. 2014, *MNRAS*, 439, 1337, doi: [10.1093/mnras/stt2468](https://doi.org/10.1093/mnras/stt2468)

- Pannella, M., Carilli, C. L., Daddi, E., et al. 2009, *ApJL*, 698, L116, doi: [10.1088/0004-637X/698/2/L116](https://doi.org/10.1088/0004-637X/698/2/L116)
- Pannella, M., Elbaz, D., Daddi, E., et al. 2015, *ApJ*, 807, 141, doi: [10.1088/0004-637X/807/2/141](https://doi.org/10.1088/0004-637X/807/2/141)
- Parente, M., Narayanan, D., & Torrey, P. 2026, arXiv e-prints, arXiv:2604.06314, doi: [10.48550/arXiv.2604.06314](https://doi.org/10.48550/arXiv.2604.06314)
- Pfarr, J., Maraston, C., & Tonini, C. 2012, *MNRAS*, 422, 3285, doi: [10.1111/j.1365-2966.2012.20848.x](https://doi.org/10.1111/j.1365-2966.2012.20848.x)
- Pillepich, A., Springel, V., Nelson, D., et al. 2018, *MNRAS*, 473, 4077, doi: [10.1093/mnras/stx2656](https://doi.org/10.1093/mnras/stx2656)
- Popping, G., Somerville, R. S., & Galametz, M. 2017, *MNRAS*, 471, 3152, doi: [10.1093/mnras/stx1545](https://doi.org/10.1093/mnras/stx1545)
- Popping, G., Pillepich, A., Calistro Rivera, G., et al. 2022, *MNRAS*, 510, 3321, doi: [10.1093/mnras/stab3312](https://doi.org/10.1093/mnras/stab3312)
- Price, S. H., Kriek, M., Brammer, G. B., et al. 2014, *ApJ*, 788, 86, doi: [10.1088/0004-637X/788/1/86](https://doi.org/10.1088/0004-637X/788/1/86)
- Puglisi, A., Rodighiero, G., Franceschini, A., et al. 2016, *A&A*, 586, A83, doi: [10.1051/0004-6361/201526782](https://doi.org/10.1051/0004-6361/201526782)
- Qin, J., Zheng, X. Z., Wuyts, S., Pan, Z., & Ren, J. 2019, *ApJ*, 886, 28, doi: [10.3847/1538-4357/ab4a04](https://doi.org/10.3847/1538-4357/ab4a04)
- Reddy, N. A., Topping, M. W., Sanders, R. L., Shapley, A. E., & Brammer, G. 2023, *ApJ*, 948, 83, doi: [10.3847/1538-4357/acc869](https://doi.org/10.3847/1538-4357/acc869)
- Reddy, N. A., Kriek, M., Shapley, A. E., et al. 2015, *ApJ*, 806, 259, doi: [10.1088/0004-637X/806/2/259](https://doi.org/10.1088/0004-637X/806/2/259)
- Reddy, N. A., Shapley, A. E., Sanders, R. L., et al. 2026, *ApJ*, 999, 15, doi: [10.3847/1538-4357/ae38da](https://doi.org/10.3847/1538-4357/ae38da)
- R emy-Ruyer, A., Madden, S. C., Galliano, F., et al. 2014, *A&A*, 563, A31, doi: [10.1051/0004-6361/201322803](https://doi.org/10.1051/0004-6361/201322803)
- Renzini, A., & Peng, Y.-j. 2015, *ApJL*, 801, L29, doi: [10.1088/2041-8205/801/2/L29](https://doi.org/10.1088/2041-8205/801/2/L29)
- Rezaee, S., Reddy, N., Shivaeei, I., et al. 2021, *MNRAS*, 506, 3588, doi: [10.1093/mnras/stab1885](https://doi.org/10.1093/mnras/stab1885)
- Rieke, M. J., Robertson, B., Tacchella, S., et al. 2023, *ApJS*, 269, 16, doi: [10.3847/1538-4365/acf44d](https://doi.org/10.3847/1538-4365/acf44d)
- Robertson, B. E., Johnson, B. D., Tacchella, S., et al. 2026, arXiv e-prints, arXiv:2601.15956, doi: [10.48550/arXiv.2601.15956](https://doi.org/10.48550/arXiv.2601.15956)
- Rodighiero, G., Edes Esposito, G., Calzetti, D., et al. 2026, arXiv e-prints, arXiv:2604.09763, doi: [10.48550/arXiv.2604.09763](https://doi.org/10.48550/arXiv.2604.09763)
- Roper, W. J., Lovell, C. C., Vijayan, A. P., et al. 2022, *MNRAS*, 514, 1921, doi: [10.1093/mnras/stac1368](https://doi.org/10.1093/mnras/stac1368)
- Salim, S., Boquien, M., & Lee, J. C. 2018, *ApJ*, 859, 11, doi: [10.3847/1538-4357/aabf3c](https://doi.org/10.3847/1538-4357/aabf3c)
- Salim, S., & Narayanan, D. 2020, *ARA&A*, 58, 529, doi: [10.1146/annurev-astro-032620-021933](https://doi.org/10.1146/annurev-astro-032620-021933)
- Salim, S., Lee, J. C., Janowiecki, S., et al. 2016, *ApJS*, 227, 2, doi: [10.3847/0067-0049/227/1/2](https://doi.org/10.3847/0067-0049/227/1/2)
- Sanders, R. L., Shapley, A. E., Jones, T., et al. 2021, *ApJ*, 914, 19, doi: [10.3847/1538-4357/abf4c1](https://doi.org/10.3847/1538-4357/abf4c1)
- Sandles, L., D'Eugenio, F., Maiolino, R., et al. 2024, *A&A*, 691, A305, doi: [10.1051/0004-6361/202347119](https://doi.org/10.1051/0004-6361/202347119)
- Schlafly, E. F., & Finkbeiner, D. P. 2011, *ApJ*, 737, 103, doi: [10.1088/0004-637X/737/2/103](https://doi.org/10.1088/0004-637X/737/2/103)
- Scholtz, J., Carniani, S., Parlanti, E., et al. 2025a, arXiv e-prints, arXiv:2510.01034, doi: [10.48550/arXiv.2510.01034](https://doi.org/10.48550/arXiv.2510.01034)
- Scholtz, J., Maiolino, R., D'Eugenio, F., et al. 2025b, *A&A*, 697, A175, doi: [10.1051/0004-6361/202348804](https://doi.org/10.1051/0004-6361/202348804)
- Seon, K.-I., & Draine, B. T. 2016, *ApJ*, 833, 201, doi: [10.3847/1538-4357/833/2/201](https://doi.org/10.3847/1538-4357/833/2/201)
- Shapley, A. E., Sanders, R. L., Reddy, N. A., Topping, M. W., & Brammer, G. B. 2023, *ApJ*, 954, 157, doi: [10.3847/1538-4357/acea5a](https://doi.org/10.3847/1538-4357/acea5a)
- Shapley, A. E., Sanders, R. L., Salim, S., et al. 2022, *ApJ*, 926, 145, doi: [10.3847/1538-4357/ac4742](https://doi.org/10.3847/1538-4357/ac4742)
- Shen, X., Vogelsberger, M., Borrow, J., et al. 2024, *MNRAS*, 534, 1433, doi: [10.1093/mnras/stae2156](https://doi.org/10.1093/mnras/stae2156)
- Shibuya, T., Ouchi, M., & Harikane, Y. 2015, *ApJS*, 219, 15, doi: [10.1088/0067-0049/219/2/15](https://doi.org/10.1088/0067-0049/219/2/15)
- Shivaeei, I., Popping, G., Rieke, G., et al. 2022, *ApJ*, 928, 68, doi: [10.3847/1538-4357/ac54a9](https://doi.org/10.3847/1538-4357/ac54a9)
- Smith, A., Kannan, R., Tacchella, S., et al. 2022, *MNRAS*, 517, 1, doi: [10.1093/mnras/stac2641](https://doi.org/10.1093/mnras/stac2641)
- Song, J., Wang, E., Jia, C., et al. 2025, arXiv e-prints, arXiv:2512.01684, doi: [10.48550/arXiv.2512.01684](https://doi.org/10.48550/arXiv.2512.01684)
- Speagle, J. S., Steinhardt, C. L., Capak, P. L., & Silverman, J. D. 2014, *ApJS*, 214, 15, doi: [10.1088/0067-0049/214/2/15](https://doi.org/10.1088/0067-0049/214/2/15)
- Tacchella, S., Finkelstein, S. L., Bagley, M., et al. 2022, *ApJ*, 927, 170, doi: [10.3847/1538-4357/ac4cad](https://doi.org/10.3847/1538-4357/ac4cad)
- Tacconi, L. J., Genzel, R., Saintonge, A., et al. 2018, *ApJ*, 853, 179, doi: [10.3847/1538-4357/aaa4b4](https://doi.org/10.3847/1538-4357/aaa4b4)
- Tamura, N., Takato, N., Shimono, A., et al. 2016, in *Society of Photo-Optical Instrumentation Engineers (SPIE) Conference Series*, Vol. 9908, Ground-based and Airborne Instrumentation for Astronomy VI, ed. C. J. Evans, L. Simard, & H. Takami, 99081M, doi: [10.1117/12.2232103](https://doi.org/10.1117/12.2232103)
- Tasca, L. A. M., Le F evre, O., Hathi, N. P., et al. 2015, *A&A*, 581, A54, doi: [10.1051/0004-6361/201425379](https://doi.org/10.1051/0004-6361/201425379)
- Theios, R. L., Steidel, C. C., Strom, A. L., et al. 2019, *ApJ*, 871, 128, doi: [10.3847/1538-4357/aaf386](https://doi.org/10.3847/1538-4357/aaf386)
- Topping, M. W., Stark, D. P., Senchyna, P., et al. 2024, *MNRAS*, 529, 3301, doi: [10.1093/mnras/stae682](https://doi.org/10.1093/mnras/stae682)
- Tremonti, C. A., Heckman, T. M., Kauffmann, G., et al. 2004, *ApJ*, 613, 898, doi: [10.1086/423264](https://doi.org/10.1086/423264)

- Tsujita, A., Fujimoto, S., Faisst, A., et al. 2026, *ApJ*, 997, 319, doi: [10.3847/1538-4357/ae22d8](https://doi.org/10.3847/1538-4357/ae22d8)
- Viero, M. P., Monceli, L., Quadri, R. F., et al. 2013, *ApJ*, 779, 32, doi: [10.1088/0004-637X/779/1/32](https://doi.org/10.1088/0004-637X/779/1/32)
- Vijayan, A. P., Thomas, P. A., Lovell, C. C., et al. 2024, *MNRAS*, 527, 7337, doi: [10.1093/mnras/stad3594](https://doi.org/10.1093/mnras/stad3594)
- Weingartner, J. C., & Draine, B. T. 2001, *ApJ*, 548, 296, doi: [10.1086/318651](https://doi.org/10.1086/318651)
- Werle, A., Cid Fernandes, R., Vale Asari, N., et al. 2019, *MNRAS*, 483, 2382, doi: [10.1093/mnras/sty3264](https://doi.org/10.1093/mnras/sty3264)
- Whitaker, K. E., Pope, A., Cybulski, R., et al. 2017, *ApJ*, 850, 208, doi: [10.3847/1538-4357/aa94ce](https://doi.org/10.3847/1538-4357/aa94ce)
- Wijesekera, J. V., Koprowski, M. P., Dunlop, J. S., et al. 2026, arXiv e-prints, arXiv:2602.04765, doi: [10.48550/arXiv.2602.04765](https://doi.org/10.48550/arXiv.2602.04765)
- Wild, V., Charlot, S., Brinchmann, J., et al. 2011, *MNRAS*, 417, 1760, doi: [10.1111/j.1365-2966.2011.19367.x](https://doi.org/10.1111/j.1365-2966.2011.19367.x)
- Witt, A. N., & Gordon, K. D. 2000, *ApJ*, 528, 799, doi: [10.1086/308197](https://doi.org/10.1086/308197)
- Woodrum, C., Shivaee, I., Witstok, J., et al. 2025, arXiv e-prints, arXiv:2510.00235, doi: [10.48550/arXiv.2510.00235](https://doi.org/10.48550/arXiv.2510.00235)
- Wright, E. L., Eisenhardt, P. R. M., Mainzer, A. K., et al. 2010, *AJ*, 140, 1868, doi: [10.1088/0004-6256/140/6/1868](https://doi.org/10.1088/0004-6256/140/6/1868)
- Wuyts, S., Förster Schreiber, N. M., Nelson, E. J., et al. 2013, *ApJ*, 779, 135, doi: [10.1088/0004-637X/779/2/135](https://doi.org/10.1088/0004-637X/779/2/135)
- Xue, Y. Q., Luo, B., Brandt, W. N., et al. 2016, *ApJS*, 224, 15, doi: [10.3847/0067-0049/224/2/15](https://doi.org/10.3847/0067-0049/224/2/15)
- Yanagisawa, H., Ouchi, M., Nakajima, K., et al. 2024, *ApJ*, 974, 180, doi: [10.3847/1538-4357/ad7097](https://doi.org/10.3847/1538-4357/ad7097)
- York, D. G., Adelman, J., Anderson, Jr., J. E., et al. 2000, *AJ*, 120, 1579, doi: [10.1086/301513](https://doi.org/10.1086/301513)
- Zahid, H. J., Kudritzki, R.-P., Conroy, C., Andrews, B., & Ho, I.-T. 2017, *ApJ*, 847, 18, doi: [10.3847/1538-4357/aa88ae](https://doi.org/10.3847/1538-4357/aa88ae)